ARTICLE

Material properties of phase-separated TFEB condensates regulate the autophagy-lysosome pathway

Zheng Wang[1], Di Chen[1,2], Dongshi Guan[3] ⓘ, Xiaobo Liang[2,4] ⓘ, Jianfeng Xue[5], Hongyu Zhao[1], Guangtao Song[2,4], Jizhong Lou[2,4] ⓘ, Yan He[5], and Hong Zhang[1,2] ⓘ

Very little is known about how the material properties of protein condensates assembled via liquid–liquid phase separation (LLPS) are maintained and affect physiological functions. Here we show that liquid-like condensates of the transcription factor TFEB exhibit low fusion propensity in vitro and in living cells. We directly measured the attraction force between droplets, and we characterized the interfacial tension, viscosity, and elasticity of TFEB condensates. TFEB condensates contain rigid interfacial boundaries that govern their interaction behaviors. Several small molecules, including Ro-3306, modify the material properties of TFEB condensates, increasing their size and fusion propensity. These compounds promote lysosomal biogenesis and function in a TFEB-dependent manner without changing its cytoplasmic-nuclear translocation. Ro-3306 promotes autophagy activity, facilitating degradation of toxic protein aggregates. Our study helps explain how protein condensates are maintained as physically separate entities and reveals that the material properties of TFEB condensates can be harnessed to modulate TFEB activity.

Introduction

The lysosome-mediated autophagy degradation system involves engulfment of unselected cytosolic material or selected cargoes such as protein aggregates, damaged organelles, and pathogens in the double-membrane autophagosome and their subsequent delivery to lysosomes for degradation (Mizushima et al., 2011; Nakatogawa, 2020; Zhao and Zhang, 2018). Autophagosome formation involves a series of sequential membrane remodeling processes, including initiation of the isolation membrane and its subsequent expansion and closure. In multicellular organisms, nascent autophagosomes fuse with endolysosomal vesicles to form amphisomes, a process known as autophagosome maturation, before autolysosomes become degradative (Mizushima et al., 2011; Zhao and Zhang, 2019). Dysfunction of autophagosome maturation has been causally associated with the pathogenesis of various human diseases such as neurodegenerative diseases, Vici syndrome, and myopathies (Cortes et al., 2014; Zhao et al., 2021). Therefore, manipulating the autophagy-lysosome pathway may provide an effective strategy for combating related diseases.

The MiT/TFE family transcription factors TFEB and TFE3 are master regulators controlling the expression of a network of genes that serve in the biogenesis and function of autophagosomes and lysosomes (Raben and Puertollano, 2016; Settembre et al., 2011). Various stresses such as energy deprivation, ER stress, mitochondrial stress, endolysosomal damage, and pathogen invasion act via different kinases and phosphatases to reduce TFEB/TFE3 phosphorylation, which facilitates their cytoplasmic-nuclear transport (Li et al., 2016; Martina and Puertollano, 2018; Medina et al., 2015; Nakamura et al., 2020; Puertollano et al., 2018; Raben and Puertollano, 2016; Settembre et al., 2012). Increasing TFEB activity appears to be effective in ameliorating the pathogenesis of various diseases, including Alzheimer's disease, Parkinson's disease, Huntington's disease, and lysosomal storage diseases (Cortes et al., 2014; Decressac et al., 2013; Li et al., 2016; Martini-Stoica et al., 2016; Song et al., 2021). Current approaches to activate TFEB are based on increasing its nuclear level via virus-mediated TFEB overexpression or modulating the activity of upstream kinases and phosphatases (Song et al., 2021).

....
[1]National Laboratory of Biomacromolecules, CAS Center for Excellence in Biomacromolecules, Institute of Biophysics, Chinese Academy of Sciences, Beijing, China;   [2]College of Life Sciences, University of Chinese Academy of Sciences, Beijing, China;   [3]State Key Laboratory of Nonlinear Mechanics, Institute of Mechanics, Chinese Academy of Sciences, Beijing, China;   [4]Key Laboratory of RNA Biology, CAS Center for Excellence in Biomacromolecules, Institute of Biophysics, Chinese Academy of Sciences, Beijing, China;   [5]Department of Chemistry, Key Laboratory of Bioorganic Phosphorus Chemistry & Chemical Biology (Ministry of Education), Tsinghua University, Beijing, China.

Correspondence to Hong Zhang: hongzhang@ibp.ac.cn.

Protein liquid–liquid phase separation (LLPS) involves concentration of constituent proteins into distinct compartments with liquid properties. These phase-separated condensates participate in a variety of cellular activities such as signal transduction, protein quality control, and gene expression (Banani et al., 2017; Boeynaems et al., 2018; Shin and Brangwynne, 2017; Zhao and Zhang, 2020). Protein condensates assembled via LLPS undergo phase transition into less dynamic hydrogel-like and solid structures (Kaganovich, 2017). The material properties of protein condensates are critical for fulfilling distinct functions (Kaganovich, 2017). Liquid-like condensates facilitate signal transduction (Su et al., 2016), and the gel-like state of protein aggregates is essential for triggering the formation of surrounding autophagosomal membranes (Noda et al., 2020; Zhang et al., 2018; Zhao and Zhang, 2020). Material properties of protein condensates such as interfacial tension and viscosity have been extensively characterized for liquid-like condensates that readily fuse, such as nucleoli and *Caenorhabditis elegans* germline P granules (Brangwynne et al., 2009; Feric et al., 2016). Certain types of condensates, such as transcriptional condensates, exhibit some liquid-like properties, such as high internal dynamics, yet are maintained as physically separate entities in compact nuclei (Boija et al., 2018; Cho et al., 2018; Chong et al., 2018; Hnisz et al., 2017; Kwon et al., 2013; Sabari et al., 2018). The underlying mechanism specifying the formation of such condensates remains largely unknown, in part owing to the lack of approaches to measure their biophysical properties. TFEB, like other transcription factors, undergoes LLPS to form transcriptional condensates for gene expression (Chen et al., 2020). TFEB nuclear condensates, which exhibit high internal dynamics, are colocalized with the transcriptional Mediator complex and associated with target mRNAs (Chen et al., 2020). LLPS of nuclear TFEB is inhibited by the nuclear chaperone protein inositol polyphosphate multikinase (IPMK; Chen et al., 2020). IPMK depletion results in the formation of more TFEB condensates and promotes autophagy activity and lysosomal biogenesis and function (Chen et al., 2020). Thus, modulation of LLPS of nuclear TFEB emerges as a novel mechanism to regulate TFEB activity without altering its subcellular distribution.

Here we used several techniques to characterize the material properties of TFEB condensates. We revealed that TFEB condensates contain rigid interfacial boundaries that determine their low fusion propensity in vitro and in living cells. By screening a chemical library, we identified several compounds that change the material properties of TFEB condensates. The identified molecules increase the activity of TFEB without altering its subcellular distribution. One of the compounds, Ro-3306, greatly enhances lysosomal biogenesis and function and promotes autophagic degradation of cytotoxic protein aggregates such as polyQ aggregates. Our study revealed that the material properties of TFEB condensates can be manipulated to regulate the autophagy-lysosome pathway.

Results

TFEB condensates exhibit low fusion propensity in in vitro LLPS assays and also in living cells

TFEB condensates formed in in vitro LLPS assays and in living cells exhibit high internal dynamics and are dissolved by 1,6-hexanediol (Chen et al., 2020), indicating that they possess liquid-like properties. Under normal growth conditions, TFEB is predominantly localized in the cytoplasm, but it undergoes nuclear transport and forms numerous puncta under autophagy induction conditions such as stresses or chemical treatment (e.g., with the mTOR inhibitor Torin 1; Puertollano et al., 2018; Chen et al., 2020). Interestingly, time-lapse analysis revealed that the condensates formed by nuclear TFEB and the related factor TFE3 rarely underwent fusion with time (Fig. 1, A and B; and Fig. S1 A). In contrast, PGL-3-GFP, a component of P granules, formed puncta in the cytoplasm of HeLa cells and underwent extensive fusion, resulting in the formation of large condensates (Figs. 1 B and S1 B).

We next determined whether TFEB condensates formed in in vitro LLPS assays also show low fusion propensity. Purified recombinant TFEB protein, which is soluble when tagged with the solubility-enhancing maltose-binding protein (MBP), underwent LLPS upon cleavage of the MBP tag by protease 3C. To facilitate our analysis of droplet behaviors, we used small droplets formed by 20 µM TFEB for 2 min in buffer containing 200 mM NaCl (Fig. S1 C; Chen et al., 2020). Unlike droplets formed by PGL-3, which underwent extensive fusion (Fig. S1, D and E; Zhang et al., 2018), the size of TFEB droplets was only slightly increased 10 min after phase induction. From 10 min to 1 h after induction, droplets remained unchanged in size and aggregated together into clusters, a process known as flocculation (Fig. S1 C). Time-lapse analysis of sulfo-Cy3–labeled TFEB droplets revealed that the droplets gradually grew with time and then stabilized ~10 min after induction (Fig. 1 C). Fusion between two encountering droplets was rarely detected (Fig. 1, D and L). In FRAP assays on TFEB droplets 2 min and 1 h after induction, the TFEB fluorescence signal quickly recovered after bleaching, and there was no evident difference between the growing and stable droplets (Fig. S1, F–H). This suggests that the low fusion propensity of TFEB droplets is not simply caused by liquid-to-gel/solid transition.

We then applied optical tweezers to directly measure the contact force between two droplets. A droplet was held by suction on the tip of a micropipette, and another was trapped by focused laser beams. The trapped droplet was moved so that the two droplets were repeatedly pushed together and then pulled apart (Fig. 1 E). The force between the two droplets during the approach and retraction phases was measured. The readily fusing PGL-3 droplets were used as controls. Two PGL-3 droplets were pushed against each other to apply pressure. From the point where the two droplets first contacted (displacement = 0 nm), a gradually elevated repulsive force was observed as the droplets were squeezed together (Fig. 1 F, red curve). Then the boundaries of the droplets at the contact interface disappeared at approximately –1,000-nm indentation, and the two droplets began to fuse into a larger one. The newly formed larger droplet tended to shrink to a sphere because of interfacial tension. The forces between the two droplets changed continuously: the magnitude of the repulsive force decreased, and eventually an attractive force occurred in response to the shrinkage of the fused PGL-3 droplets (Fig. 1 F, cyan curve). At that point, the optical tweezers were pulled back. As the two droplets had fused into a larger one, the single droplet trapped by the optical
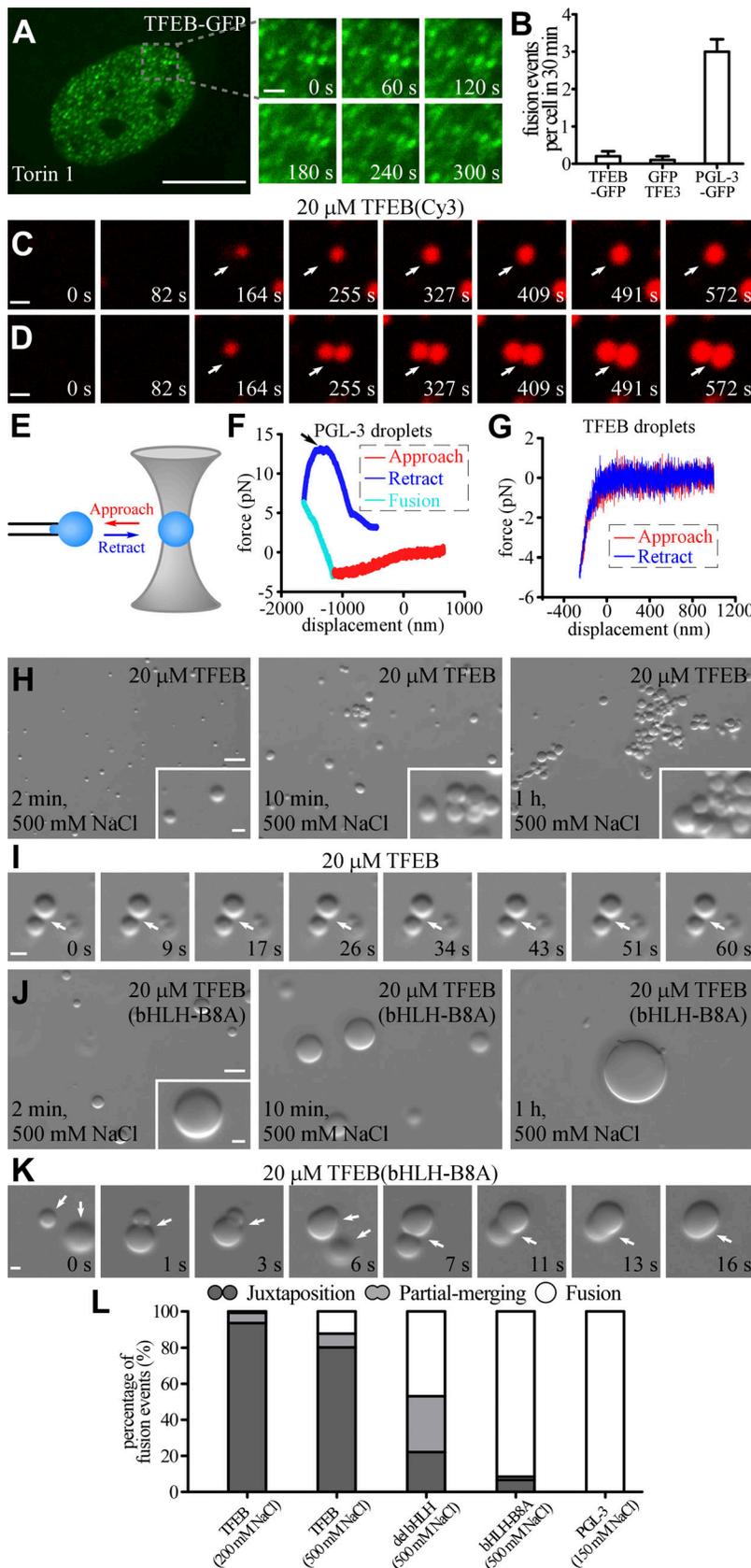
Figure 1. **TFEB forms phase-separated condensates with low fusion propensity. (A and B)** Time-lapse analysis showing that the nuclear TFEB-GFP puncta in Torin 1–treated HeLa cells rarely fuse with each other (A). Quantification of fusion events in each cell during a 30 min period for TFEB-GFP, GFP-TFE3, and PGL-3-GFP droplets (B). Data are shown as mean ± SEM (*n* = 10 cells for each bar) in B. **(C and D)** Cy3-labeled TFEB droplets grow with time (white arrow) in a buffer containing 200 mM NaCl (C). Upon encounter (white arrow), two TFEB droplets fail to fuse during the period of examination (D). The time refers to imaging time, and the time point of the first image is defined as 0 s. **(E)** Schematic for the optical tweezers experiments. A single droplet is held on a micropipette by suction, and another droplet is trapped by the optical tweezers. The force between the two droplets during multiple approach and retraction phases is measured by the optical tweezers and recorded. Droplets with a diameter of ∼5–10 μm were used for the experiments. **(F and G)** Representative force–displacement curves recording the force between two PGL-3 droplets formed in 150 mM NaCl buffer (F) or TFEB droplets formed in 500 mM NaCl buffer (G) during approach and retraction. Repulsive forces are detected when two PGL-3 droplets get close. The two PGL-3 droplets fuse together at approximately −1,000 nm, and the repulsive forces gradually convert to attractive forces due to shrinkage of the fused droplets. At the top of the blue curve (arrow), the optical tweezers fell off the trapped droplet (F). No obvious forces are detected before contact between two TFEB droplets (G). The indentations on TFEB droplets are much smaller than on PGL-3 droplets at the force of approximately −4 pN, which suggests that TFEB droplets are much harder than PGL-3 droplets. **(H and I)** DIC images showing that 20 μM TFEB forms droplets in 500 mM NaCl buffer 2 min after LLPS induction. The size of droplets remains unchanged from 10 min to 1 h after induction. The droplets gradually cluster with time (H). Time-lapse images of two encountering TFEB droplets that do not undergo fusion with time (I; arrows). The time point of the first image is defined as 0 s. **(J and K)** DIC images showing that 20 μM TFEB(bHLH-B8A) forms droplets in 500 mM NaCl buffer from 2 min to 1 h after LLPS induction (J). The droplets continuously fuse upon encounter, resulting in formation of large droplets (J). Time-lapse images of three encountering TFEB(bHLH-B8A) droplets which undergo rapid fusion (K; arrows). The time point of the first image is defined as 0 s. **(L)** Percentage of fusion events for droplets formed by 20 μM wild-type and mutant TFEB and 10 μM PGL-3 in the indicated salt buffers. Three types of event (juxtaposition, partial merging, and fusion) are defined for droplets that underwent an encounter for 30 s. 124, 106, 113, 106, and 100 fusion events were analyzed for TFEB in 200 and 500 mM NaCl buffer; TFEB(del bHLH) and TFEB(bHLH-B8A) in 500 mM NaCl; and PGL-3 in 150 mM NaCl, respectively. Scale bars: 10 μm (A); 5 μm (H and J); 1 μm (C, D, I, and K); 1 μm (enlarged figures in A and insets in H and J).

tweezers could not be separated, and the attractive forces kept increasing during the retraction process until the optical tweezers fell off (Fig. 1 F, blue curve). However, no force was detected between two TFEB droplets during the approach or retraction phases (Fig. 1 G). The repulsive force between two TFEB droplets increased much faster than in PGL-3 droplets as the indentation deepened, which suggests that TFEB droplets are harder and more elastic than PGL-3 droplets. Therefore, although TFEB droplets exhibit liquid-like properties, they show low propensity for fusion.

The charged residues in the bHLH domain specify the fusion propensity of TFEB condensates in in vitro LLPS assays and also in living cells

LLPS of protein condensates is mediated by hydrophobic and/or charge-based interactions. Electrostatic interactions are strongly influenced by increasing the ionic strength of a solution (Nott et al., 2015). TFEB failed to undergo phase separation in 50 mM salt buffer (Fig. S1 I). When the salt concentration in the buffer was increased from 100 to 1,000 mM, TFEB gradually underwent LLPS, and the droplet size increased (Fig. S1, I–K). TFEB droplets in 500 mM salt grew larger than those in 200 mM salt (Fig. S1 L), and small TFEB droplets sometimes underwent fusion upon contact (Fig. S1 M). Beyond a size of ∼1 µm, fusion of TFEB droplets in 500 mM NaCl was rarely detected, and the droplets formed aggregates (Fig. 1, H, I, and L). Surprisingly, increasing the salt concentration also reduced the critical concentration for TFEB to undergo LLPS (Fig. S1 K), which could be because of salting out of the hydrophobic regions. In living cells, TFEB-GFP was diffusely distributed in the cytoplasm (Fig. S1 N). When the growth medium was supplemented with 300 mM NaCl, cells survived for several hours, and TFEB-GFP formed a large number of puncta in the cytoplasm (Fig. S1, O and P). Upon refeeding the cells with normal growth medium, the cytoplasmic TFEB puncta disappeared within 1 min (Fig. S1 Q). Thus, a change in ionic strength affects LLPS of TFEB both in vitro and in living cells.

TFEB contains a bHLH domain, which is required for its nuclear translocation and DNA binding (Fig. S1 R). TFEB with a deletion of the bHLH domain, TFEB(del bHLH), failed to undergo phase separation even at a concentration of 40 µM in a 200-mM salt buffer (Fig. S1 S). High salt also facilitated LLPS of TFEB(del bHLH) (Fig. S1 T). In 500 mM salt, 20 µM TFEB(del bHLH) formed droplets that fused extensively until they reached a size of ∼2 µm, at which stage the fusion speed slowed down (Figs. 1 L and S1 U). We further examined the effect of charged residues in the bHLH domain on the fusion of TFEB condensates (Fig. S1 R). Mutating the positively charged residues in the bHLH domain impaired LLPS of TFEB, as shown by sedimentation assays (Fig. S1 V). Formation of droplets was gradually suppressed upon mutation of two, four, or six basic residues in the bHLH domain (Fig. S1 W). 20 µM TFEB with mutations of eight basic bHLH residues (TFEB[bHLH-B8A]) failed to undergo LLPS in a 200 mM NaCl buffer but formed droplets in a 500 mM NaCl buffer (Figs. 1 J and S1 X). TFEB(bHLH-B8A) droplets underwent extensive fusion after induction, resulting in formation of larger droplets, which even reached sizes of ∼10 µm (Fig. 1, J–L).

Droplets >10 µm flocculated without fusion (Fig. S1 Y). Thus, the charged residues in the bHLH domain modulate LLPS and also the fusion properties of TFEB droplets.

We further determined the role of the charged residues in formation of TFEB puncta in living cells. In Torin 1–treated cells, nuclear TFEB(bHLH-B2A)-GFP puncta were larger than TFEB-GFP puncta (Fig. 2, A, B, and E). TFEB(bHLH-B8A)-GFP showed no nuclear localization owing to mutations in the NLS. TFEB(bHLH-B8A)-GFP-NLS, in which an NLS was added, formed puncta in the nucleus upon Torin 1 treatment (Fig. 2, C and D). TFEB(bHLH-B8A)-GFP-NLS recovered quickly after bleaching in the FRAP assay (Fig. 2, F–H). Compared to TFEB-GFP-NLS puncta, which were similar to TFEB-GFP, TFEB(bHLH-B8A)-GFP-NLS puncta were much larger and underwent more fusion events (Fig. 2, C–E and I–L). Therefore, the charged residues in bHLH modulate the fusion propensity of TFEB in living cells.

TFEB droplets exhibit high interfacial tension and rigid interfacial boundaries

We showed above that TFEB droplets flocculate into large clusters with time, even though they fail to fuse in the time scale of observation. To investigate the mechanism underlying the unique behaviors of TFEB condensates, we used a series of assays to characterize the biophysical properties of TFEB condensates formed in vitro. The interfacial tension of dispersed phases, which reflects the excess energy at the interface, tends to drive interfaces to adopt geometries that minimize the area of interface and also to undergo fusion or flocculation to minimize the surface free energy (Tadros, 2013). We adapted the micropipette aspiration (MPA) technique, which is based on analysis of pressure differentials across curved interfaces (Fig. 3 A; Drelich et al., 2002), to measure the interfacial tension of protein condensates. A droplet was first captured at the tip of a glass micropipette, and the minimum pressure at which the droplet extended a protrusion into the pipette was determined. The interfacial tension γ is calculated with the following function: $\gamma = \Delta P/2(1/R_P - 1/R_D)$. ΔP, R_P, and R_D represent the negative pressure, the inner radius of the micropipette, and the radius of the droplet, respectively. The calculated interfacial tension was $8.54 \pm 0.33 \times 10^{-4}$ and $7.71 \pm 0.25 \times 10^{-5}$ N/m (mean ± SEM) for the wild-type TFEB and TFEB(bHLH-B8A) droplets, respectively (Fig. 3, B and C). The interfacial tension of PGL-3 droplets is below the limits detected by MPA (∼3×10^{-6} N/m). These results indicate that TFEB droplets are not stably dispersed but tend to associate with each other in the phase-separated system.

Coalescence of two contacting droplets involves the deformation, thinning, disruption, and eventual rupture of the interfacial boundary and mixing of internal constituents (Tadros, 2013). Therefore, the viscosity and elasticity of the interfacial boundary determines the stability of droplets (see Materials and methods for detailed theory; Biswas and Haydon, 1963; Tadros, 2013). The higher the viscosity, the longer it will take to deform a drop for coalescence. Higher elasticity indicates stronger resistance to droplet deformation, which contributes to disruption and rupture of interfacial boundaries. We used single gold nanorods (AuNRs) as rotational microrheology probes to
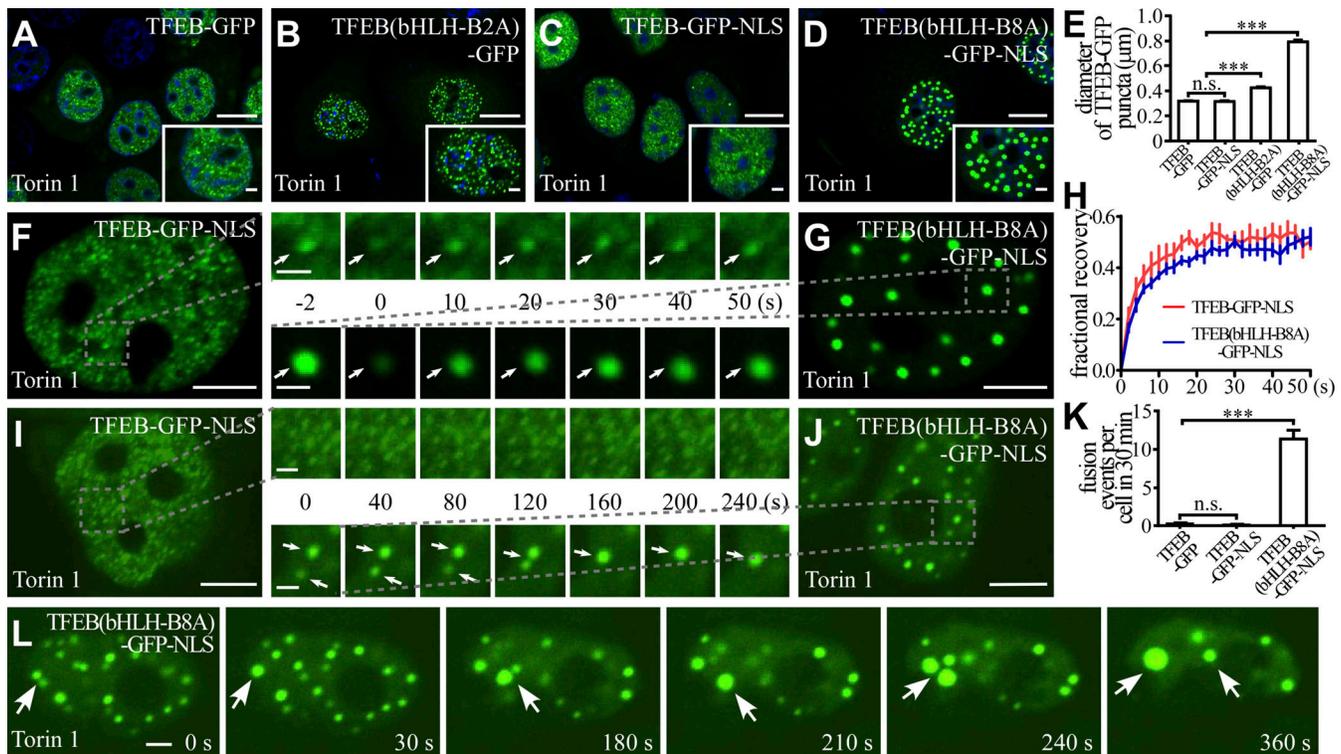
Figure 2. **The effect of charged residues in the bHLH domain on the formation and biophysical properties of TFEB puncta in living cells. (A–E)** Puncta formed by expressing wild-type or mutant TFEB-GFP and TFEB-GFP-NLS upon Torin 1 treatment in the nucleus of HeLa cells. Compared with TFEB-GFP puncta (A), the TFEB(bHLH-B2A)-GFP puncta are larger (B). The size of TFEB-GFP-NLS puncta is similar to TFEB-GFP puncta (C), while the size of TFEB(bHLH-B8A)-GFP-NLS droplets is much larger (D). Quantification of the diameter of nuclear wild-type or mutant TFEB-GFP and TFEB-GFP-NLS puncta (E). The biggest 10 puncta in each cell were chosen, and the diameters were measured by ImageJ. Data are shown as mean ± SEM (n = 100 puncta for each bar). ***, P < 0.001. **(F–H)** FRAP analysis of the TFEB-GFP-NLS (F) and TFEB(bHLH-B8A)-GFP-NLS (G) signals of the punctate structures (arrows) in the nucleus of Torin 1–treated HeLa cells. Quantification of the FRAP data for F and G (H). Data are shown as mean ± SEM (n = 3) in H. **(I–K)** Time-lapse experiments showing that TFEB-GFP-NLS puncta rarely fuse with each other (I), while TFEB(bHLH-B8A)-GFP-NLS puncta (arrows) undergo frequent fusion (J) in the nucleus of Torin 1–treated HeLa cells. Quantification of fusion events in each cell for 30 min for TFEB-GFP, TFEB-GFP-NLS, and TFEB(bHLH-B8A)-GFP-NLS droplets (K). Data are shown as mean ± SEM (n = 10 cells for each bar) in K. ***, P < 0.001. **(L)** Nuclear TFEB(bHLH-B8A)-GFP-NLS puncta in Torin 1–treated HeLa cells undergo continuous fusion (arrows) and become larger with time. Scale bars: 10 μm (A–D); 5 μm (F, G, I, and J); 2 μm (L and enlarged figures in F and G); 1 μm (enlarged figures in I and J and insets in A–D).

characterize the apparent viscosity of TFEB droplets (Xu et al., 2014). AuNRs with a mean size of 40 × 80 nm were packaged inside the droplets, and their translational and rotational motion trails were tracked (Fig. 3 D). We found that the speed of translation and rotation dramatically slowed when the AuNRs were close to the droplet boundary (Fig. 3, E and F). The viscosity of TFEB droplets, calculated from the rotational tracks, was 549.8 cP on the surface but only 78.8 cP in the interior (Fig. 3 F). The viscosity of TFEB(bHLH-B8A) droplets was 192.3 cP on the surface and 87.0 cP in the interior (Fig. 3 G). For PGL-3 droplets, the viscosity was 43.5 cP on the surface and 20.4 cP in the interior (Fig. 3 H). Thus, the surface viscosity and the difference between the boundary and interior are much greater in TFEB droplets than in TFEB(bHLH-B8A) and PGL-3 droplets.

The apparent elastic (Young's) modulus (E) of droplets was measured by atomic force microscopy (AFM; Fig. 3 I). The AFM probe with an adhered glass bead was gradually lowered at a constant speed toward a condensed droplet. The force generated by deformation of the droplet after compression by the probe was measured. The elastic modulus of the droplet was calculated

by fitting the slope of the approach curves using the Hertz model. The elastic modulus was 11.8, 4.0, and 1.6 kPa for TFEB, TFEB(bHLH-B8A), and PGL-3 droplets, respectively (Fig. 3, J–O). The large interfacial viscosity and elastic modulus of the TFEB droplets indicate that it is difficult for these droplets to deform and coalesce upon encounter. Taken together, these results suggest that TFEB droplets contain rigid interfacial boundaries, which explains their inefficient coalescence.

Screening of small molecular compounds that alter the material properties of TFEB condensates

We used imaging-based high-throughput screening of small molecules to identify compounds that alter the size of TFEB droplets (Fig. 4 A). The effects of the preliminary candidates on the fusion propensity of TFEB droplets were further confirmed in in vitro LLPS experiments. The activity of TFEB is controlled by its cytoplasmic-nuclear transport. To simplify our investigation into the role of the material properties of TFEB in gene regulation, we excluded compounds that induced nuclear translocation of TFEB in living cells. Ro-3306 and vanillic acid
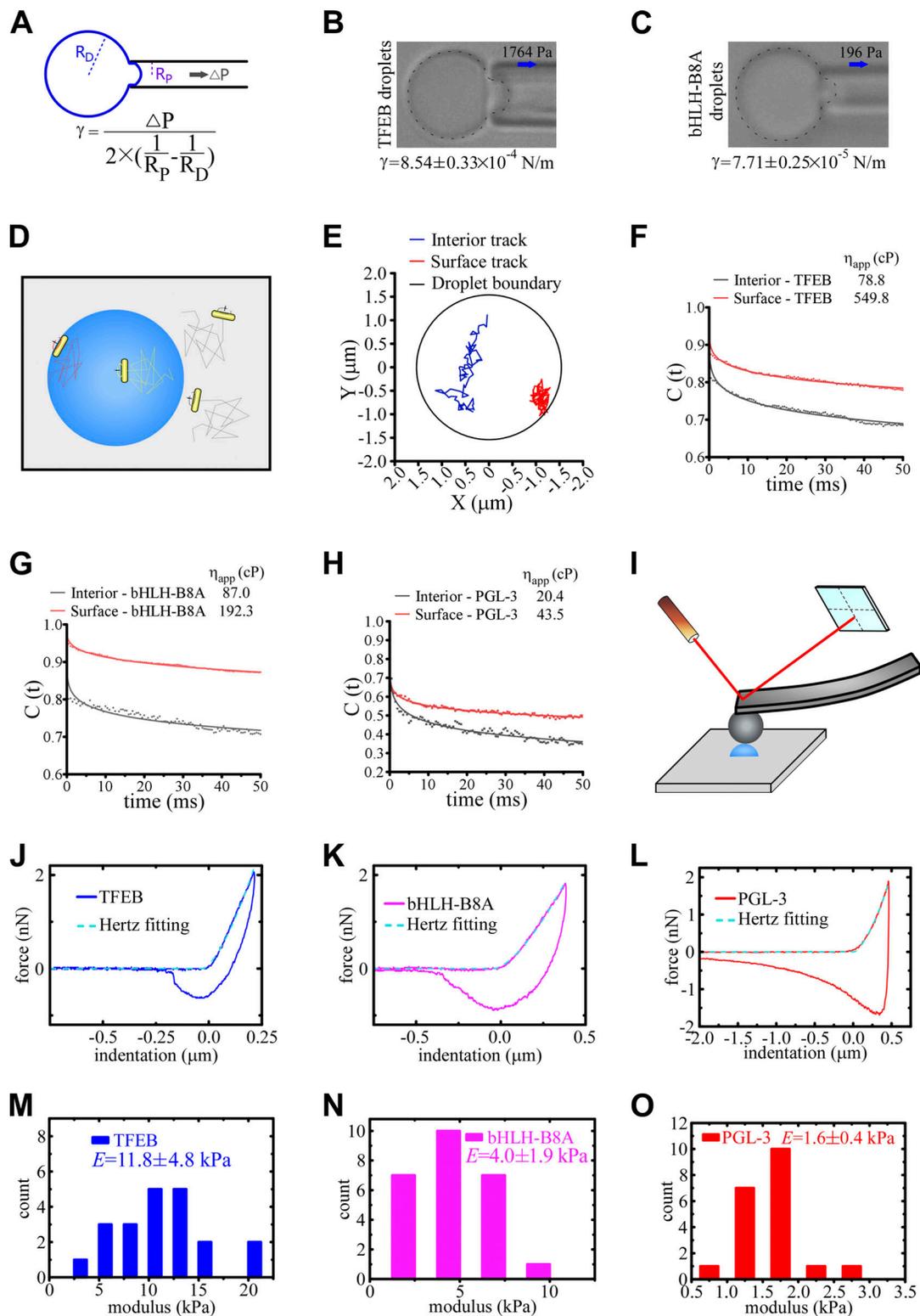
Wang et al.
Material properties of TFEB condensates

Journal of Cell Biology   5 of 21
https://doi.org/10.1083/jcb.202112024

Figure 3. The material properties of TFEB, TFEB(bHLH-B8A), and PGL-3 droplets. (A) Schematic for the measurement of the interfacial tension of droplets. Negative pressure is used to draw out the surface of a droplet. The function for calculating the interfacial tension is shown underneath. Droplets with a diameter of ~5–10 µm diluted in pre-prepared saturated protein solutions were used for the experiments. **(B and C)** Representative pictures of the micropipette experiments for TFEB (B) and TFEB(bHLH-B8A) (C) droplets formed in 500 mM NaCl buffer. 1,764 and 196 Pa of negative pressure was used to draw out the surface of TFEB and TFEB(bHLH-B8A) droplets, respectively. The direction of suction is indicated by arrows. The calculated interfacial tension is shown underneath as mean ± SEM (n = 11 and 10 for TFEB and TFEB(bHLH-B8A) droplets, respectively). **(D)** Schematic for the single-AuNR tracking experiments. The AuNRs are packaged into the droplets during LLPS induction. The trajectories of the translational and rotational Brownian diffusion of the AuNRs are recorded and analyzed to calculate the viscosity both on the surface and inside the droplets. **(E)** Trajectories of translational movements of a single AuNR in the interior

and on the surface of the same TFEB droplet formed in 500 mM NaCl buffer. The AuNR moves more freely in the interior than on the surface of the droplet. **(F–H)** Autocorrelation decay curves (solid lines) reflect the rotational behavior of AuNRs in the droplets. The calculated apparent viscosity, which is corrected with the viscosity of the solution, is shown at the top. Rotational tracks of the AuNRs in the interior and on the surface were obtained from the same droplets for TFEB (F) and TFEB(bHLH-B8A) (G) formed in 500 mM NaCl buffer, and PGL-3 droplets (H) formed in 150 mM NaCl buffer. **(I)** Schematic for the AFM experiments. A droplet (blue hemisphere) adsorbed onto a glass coverslip is tapped by an elastic probe with a known spring constant. The cantilever of the probe bends in response to the force when the probe taps the droplet, and the degree of bending is detected by a laser beam and converted to digital signals. Droplets with a diameter of ∼5–10 µm were used for the experiments. **(J–L)** The force–indentation curves measured on TFEB (J) and TFEB(bHLH-B8A) (K) droplets formed in 500 mM NaCl buffer and PGL-3 droplets formed in 150 mM NaCl buffer (L) with the approach and retraction curves as solid lines. The cyan dashed lines show the fitting of the Hertz model to the approach curves. **(M–O)** The distribution of the measured elastic modulus E of TFEB (M) and TFEB(bHLH-B8A) (N) droplets formed in 500 mM NaCl buffer and PGL-3 droplets formed in 150 mM NaCl buffer (O). The calculated elastic moduli are E = 11.8 ± 4.8, 4.0 ± 1.9, and 1.6 ± 0.4 kPa for TFEB, TFEB(bHLH-B8A), and PGL-3 droplets, respectively. Data are shown as mean ± SEM (n = 21, 25, and 20 for TFEB, TFEB(bHLH-B8A), and PGL-3 droplets, respectively).

were selected for further analysis, as they showed the most significant effect on the size and fusion propensity of TFEB droplets and on the number of lysosomes without changing the subcellular distribution of TFEB (Figs. 4 B and S2 A). In the presence of Ro-3306 and vanillic acid, the droplets formed by 20 µM TFEB (hereafter referred to as TFEB/Ro-3306 and TFEB/vanillic acid droplets) were larger in size (Fig. 4, C and D; and Fig. S2, B and C). Compared with control TFEB droplets, TFEB/Ro-3306 and TFEB/vanillic acid fused more readily in the first several dozens of minutes after induction, and then become stable and flocculated 1 h after LLPS induction (Fig. 4, C–F; and Fig. S2, C and D). These compounds failed to alter the size and fusion behaviors of TFE3 condensates, which also showed low fusion propensity (Fig. S2, E–G). Thus, these compounds do not nonselectively promote the fusion of condensates formed by transcription factors.

Ro-3306 and vanillic acid alter the material properties of TFEB condensates

We measured the material properties of TFEB/Ro-3306 and TFEB/vanillic acid droplets. Protein condensates formed by LLPS undergo phase transition to adopt a more stable material state. The material properties of TFEB condensates varied within a small range during the whole measurement process, indicating that phase transition reached equilibrium shortly after LLPS induction. We found that the material properties of TFEB/Ro-3306 and TFEB/vanillic acid droplets underwent transition over a longer period (>30 min) to reach equilibrium. The estimated interfacial tension for unstable (i.e., pre-equilibrium) TFEB/Ro-3306 and TFEB/vanillic acid droplets was <1.2 × 10⁻⁵ N/m within 30 min of induction, which is much smaller than the interfacial tension of TFEB droplets (8.54 ± 0.33 × 10⁻⁴ N/m; Figs. 4 G and S2 H). The interfacial tension was 1.81 ± 0.06 × 10⁻³ N/m and 1.22 ± 0.05 × 10⁻³ N/m, respectively, for TFEB/Ro-3306 and TFEB/vanillic acid droplets aged for 30 min (Figs. 4 H and S2 I). The AuNR measurements also indicated that TFEB/Ro-3306 and TFEB/vanillic acid droplets possessed distinct states at different times after induction. Unstable TFEB/Ro-3306 and TFEB/vanillic acid droplets have an interior viscosity of 18.2 and 23.2 cP and a surface viscosity of 192.2 and 102.2 cP, respectively, all of which are much smaller than those of TFEB droplets (Figs. 4 I and S2 J). Aged TFEB/Ro-3306 and TFEB/vanillic acid droplets have an interior viscosity of 190.8 and 149.8 cP and a surface viscosity of 1,495.0 and 1,209.0 cP, respectively, all of which are much larger

than those of TFEB droplets (Figs. 4 J and S2 K). The changes in material properties of TFEB/Ro-3306 and TFEB/vanillic acid droplets with time are consistent with their time-dependent fusion propensity in in vitro LLPS systems (Fig. 4 K).

We further examined the biophysical properties of TFEB condensates in living cells treated with Ro-3306 and vanillic acid. 10 µM of these compounds was used for experiments in living cells unless otherwise noted. The size of TFEB condensates was significantly increased by treatment with Ro-3306 and vanillic acid (Fig. 4, L–O). FRAP assays show that the molecules in TFEB/Ro-3306 and TFEB/vanillic acid condensates were less mobile than in TFEB condensates (Fig. 4, P–S). TFEB also formed lysosome-localized puncta after Torin 1 treatment (Martina and Puertollano, 2013). The puncta were immobile in FRAP assays, suggesting that they are not phase-separated liquid condensates (Fig. S2, L and M). Ro-3306 treatment also decreased the mobility of two TFEB mutants, S221A and S142A (Fig. S2, N–R), which carry mutations in mTOR-mediated phosphorylation sites and show increased nuclear localization. This suggests that the material properties of TFEB/Ro-3306 and TFEB/vanillic acid condensates in the nucleus are similar to the aged droplets assembled in the in vitro studies. Thus, Ro-3306 and vanillic acid modify the material properties of TFEB condensates.

Ro-3306 and vanillic acid promote lysosomal function and biogenesis

We next examined whether these compounds modulate the function of TFEB in regulating the function and biogenesis of lysosomes. Various stresses modulate phosphorylation of TFEB to control its cytoplasmic-nuclear transport (Puertollano et al., 2018). Both subcellular fractionation and fluorescence imaging assays showed that the nuclear TFEB level was not changed by Ro-3306 and vanillic acid treatment (Fig. 5, A–C; and Fig. S2 S). Consistent with this, the phosphorylation level of TFEB remained unchanged in Ro-3306– and vanillic acid–treated cells (Fig. 5 A). Therefore, the cytoplasmic-to-nuclear transport of TFEB was not affected by treatment with Ro-3306 and vanillic acid. TFEB is the master transcription factor regulating the function and biogenesis of lysosomes. The mRNA levels of TFEB target genes were significantly elevated in Ro-3306– and vanillic acid–treated HeLa cells (Figs. 5 D and S3 A). Thus, these chemicals promote the transcription activity of TFEB.

Lysosomal biogenesis and function were then assessed in cells treated with these chemicals. In control cells, lysosomes are
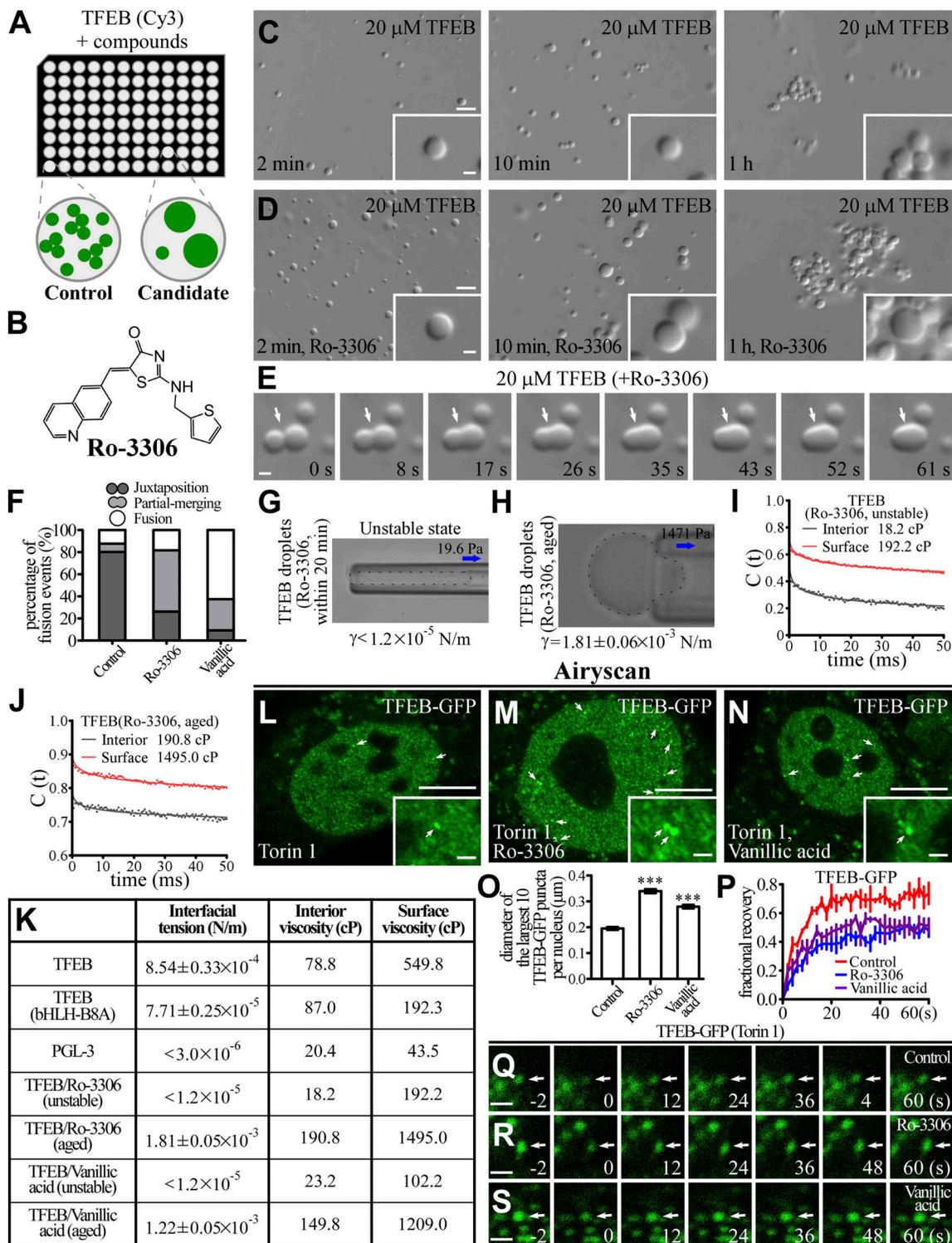
Figure 4. **Ro-3306 changes the material properties of TFEB condensates. (A)** Schematic illustration of the strategy for screening small molecular compounds that increase the size of TFEB droplets. **(B)** 2D structure of Ro-3306. **(C and D)** DIC images showing that 20 μM TFEB forms droplets in 500 mM NaCl buffer with or without 50 μM Ro-3306 2 min to 1 h after LLPS induction. **(E)** Time-lapse images of two encountering TFEB droplets undergoing fusion (arrows) in buffer containing 50 μM Ro-3306. The time point of the first image is defined as 0 s. **(F)** Percentage of fusion events for droplets formed by 20 μM TFEB in the presence of 50 μM Ro-3306 and vanillic acid in 500 mM NaCl buffer. Three types of events (juxtaposition, partial merging, and fusion) are defined for droplets that underwent an encounter for 30 s. The control data are for TFEB droplets formed in 500 mM NaCl, as shown in Fig. 1 L. 126 and 120 fusion events were analyzed for TFEB/Ro-3306 and TFEB/vanillic acid droplets, respectively. **(G and H)** Representative pictures of the micropipette experiments for newly formed (G) and aged (H) TFEB droplets formed in 500 mM NaCl buffer containing 100 μM Ro-3306. 19.6 and 1,471 Pa of negative pressure was used to draw out the surface of newly formed and aged TFEB droplets, respectively. The direction of suction is indicated by arrows. The interfacial tension for newly formed droplets is estimated and shown underneath, and the calculated interfacial tension for aged droplets is shown underneath as mean ± SEM (n = 10). The

droplet in G was not still and moved into the micropipette with time. **(I and J)** Autocorrelation decay curves (solid lines) reflect the rotational behavior of AuNRs in the droplets. The calculated apparent viscosity, which is corrected with the viscosity of the solution, is shown at the top. Rotational tracks of the AuNRs in the interior and on the surface were obtained from the same newly formed (I) and aged (J) TFEB droplets formed in 500 mM NaCl buffer containing 100 µM Ro-3306. **(K)** Summary of the measured interfacial tension and interior surface viscosity of in vitro–assembled TFEB, TFEB(bHLH-B8A), PGL-3, and unstable and aged TFEB/Ro-3306 and TFEB/vanillic acid droplets. **(L–O)** Compared with control HeLa cells stably expressing TFEB-GFP (L), nuclear TFEB-GFP puncta are evidently enlarged by incubation in 10 µM Ro-3306 (M) and vanillic acid (N). Representative TFEB-GFP puncta are pointed out by arrows in L and M. Airyscan images are shown. To facilitate the analysis, cells were treated with Torin 1 to increase the nuclear TFEB level. The few punctate structures formed by TFEB-GFP in the cytoplasm upon Torin 1 treatment correspond to TFEB that is retained on lysosomes (L–N; Martina and Puertollano, 2013). Quantification of the diameter of the largest 10 TFEB-GFP puncta per nucleus in L–N (O). Data are shown as mean ± SEM (n = 100 puncta for each bar) in O. ***, P < 0.001. **(P–S)** FRAP analysis of the TFEB-GFP–positive punctate structures (arrows) in the nucleus of control HeLa cells (Q) and HeLa cells treated with 10 µM Ro-3306 (R) and vanillic acid (S). All cells were cotreated with Torin 1. Quantification of FRAP data for Q–S (P). Data are shown as mean ± SEM (n = 3) in P. Scale bars: 10 µm (L–N); 5 µm (C and D); 1 µm (E, Q–S, and insets in C, D, and L–N).

mainly concentrated at the perinuclear region. In Ro-3306–treated cells, the number of lysosomes stained by LAMP1 antibody was dramatically increased, and the lysosomes were more scattered (Fig. 5, E and K). The LAMP1 protein level was also increased by Ro-3306 treatment (Fig. S3 B), and Ro-3306 treatment increased the number of puncta stained by Lyso-Tracker, which detects acidic lysosomes (Fig. 5, F and L). The number of fluorescent puncta containing DQ-BSA, a BSA derivative that fluoresces upon lysosomal degradation (Humphries and Payne, 2012), and the number of Magic Red puncta, which reflect the activity of the lysosomal enzyme cathepsin B (CTSB), were much greater in Ro-3306–treated cells (Fig. 5, G, H, and K). The level of mature cathepsin D (CTSD) was also increased in Ro-3306–treated cells (Fig. S3 B). Damaged lysosomes labeled by the reporter for the β-galactoside–binding cytosolic lectin Galectin-3 (GAL3) were not detected in control and Ro-3306–treated cells (Fig. S3, C and D). These results indicate that Ro-3306 treatment promotes lysosomal biogenesis and function. After Ro-3306 was washed out, the increase in LysoTracker-positive lysosomes gradually returned to the normal level within 8 h (Fig. S3 E). This indicates that Ro-3306 has a reversible effect on lysosomal biogenesis. Ro-3306 evidently enhanced lysosomal biogenesis in HeLa cells at 1 µM (Fig. S3, F and G), and it promoted lysosomal biogenesis and function in other cell lines such as COS-7 (Fig. S3, H–K). Ro-3306 is a known CDK1 inhibitor that arrests cells at the G2/M phase (Vassilev et al., 2006; Odle et al., 2020). Ro-3306 regulates lysosomal biogenesis and function independently of its role on CDK1. Less than 5% of unsynchronized cells were undergoing mitosis, shown by signals for phosphorylated histone H3 at Ser-10 (p[Ser]-H3; Juan et al., 1998), and no mitotic cells were detected upon Ro-3306 treatment (Fig. S3, L and M). Knocking down CDK1 did not change the lysosome number, nor did it affect the increased lysosome number caused by Ro-3306 (Fig. 5 L; and Fig. S3, N and O). Treatment by another CDK1 inhibitor, Dinaciclib, had no effect on lysosomal biogenesis (Figs. 5 L and S3 P). These results suggest that Ro-3306 promotes lysosomal biogenesis and function by directly activating TFEB activity.

Vanillic acid also promoted lysosome activity in terms of both number and degradation ability, but to a less dramatic extent than Ro-3306 (Fig. 5, K and L; Fig. S3 B; and Fig. S4, A–C). Like Ro-3306, the effect of vanillic acid on lysosomes was reversible (Fig. S4 D) and GFP-GAL3 puncta were absent in vanillic acid–treated cells (Fig. S3, C and D). Together, these results provide

evidence that Ro-3306 and vanillic acid reversibly promote lysosomal biogenesis and function in living cells.

TFEB is required for Ro-3306 and vanillic acid to promote lysosomal function and biogenesis

We next determined whether TFEB is required for the lysosomal phenotype caused by Ro-3306 and vanillic acid. Knocking down TFEB, but not TFE3, almost completely abolished the Ro-3306–induced promotion of lysosomal biogenesis and function shown by LysoTracker staining (Fig. 5, I, J, and L; and Fig. S3 N). The increased numbers of LysoTracker-stained structures in vanillic acid–treated cells are also dependent on TFEB (Fig. S4, E–H).

Compared with cells treated separately with Torin1 and Ro-3306/vanillic acid, the number of LAMP1-labeled late endosomes/lysosomes and LysoTracker-stained puncta was higher in cells simultaneously treated by Torin1 and Ro-3306/vanillic acid (Fig. S4, I–L), indicating that they act via distinct mechanisms to control lysosomal biogenesis.

Ro-3306 activates autophagy in a TFEB-dependent manner

We investigated whether Ro-3306 treatment promotes autophagy activity, a process involved in engulfment of cytosolic contents in the autophagosome and delivery to lysosomes for degradation (Mizushima et al., 2011; Nakatogawa, 2020; Zhao et al., 2021). The mRNA levels of autophagic genes, which are also TFEB targets, were significantly elevated in Ro-3306–treated HeLa cells (Fig. 6 A; Settembre et al., 2011). Autophagic structures are decorated with lipidated (phosphatidylethanolamine-conjugated) LC3, a ubiquitin-like autophagy protein related to yeast ATG8 (Mizushima et al., 2011). The number of autophagic structures labeled by LC3 was dramatically increased upon Ro-3306 treatment, even under nutrient-rich conditions (Fig. 6, B and C). The level of lipidated LC3 (LC3-II) was increased, while the autophagy substrate p62 was decreased, in Ro-3306–treated cells (Fig. 6 E), indicating that autophagy activity is activated by Ro-3306.

Puromycin triggers accumulation of a large number of p62-positive aggregates that can be degraded by autophagy (Eggers et al., 1997). Compared with puromycin-treated control cells, Ro-3306 dramatically reduced the number of puromycin-induced p62 aggregates (Fig. S5, A, B, E, and F). This effect of Ro-3306 was completely blocked by the lysosome inhibitor Bafilomycin A1 (Fig. S5, C–E), indicating that these aggregates are removed by the autophagy-lysosome pathway. TFEB, but not TFE3 or
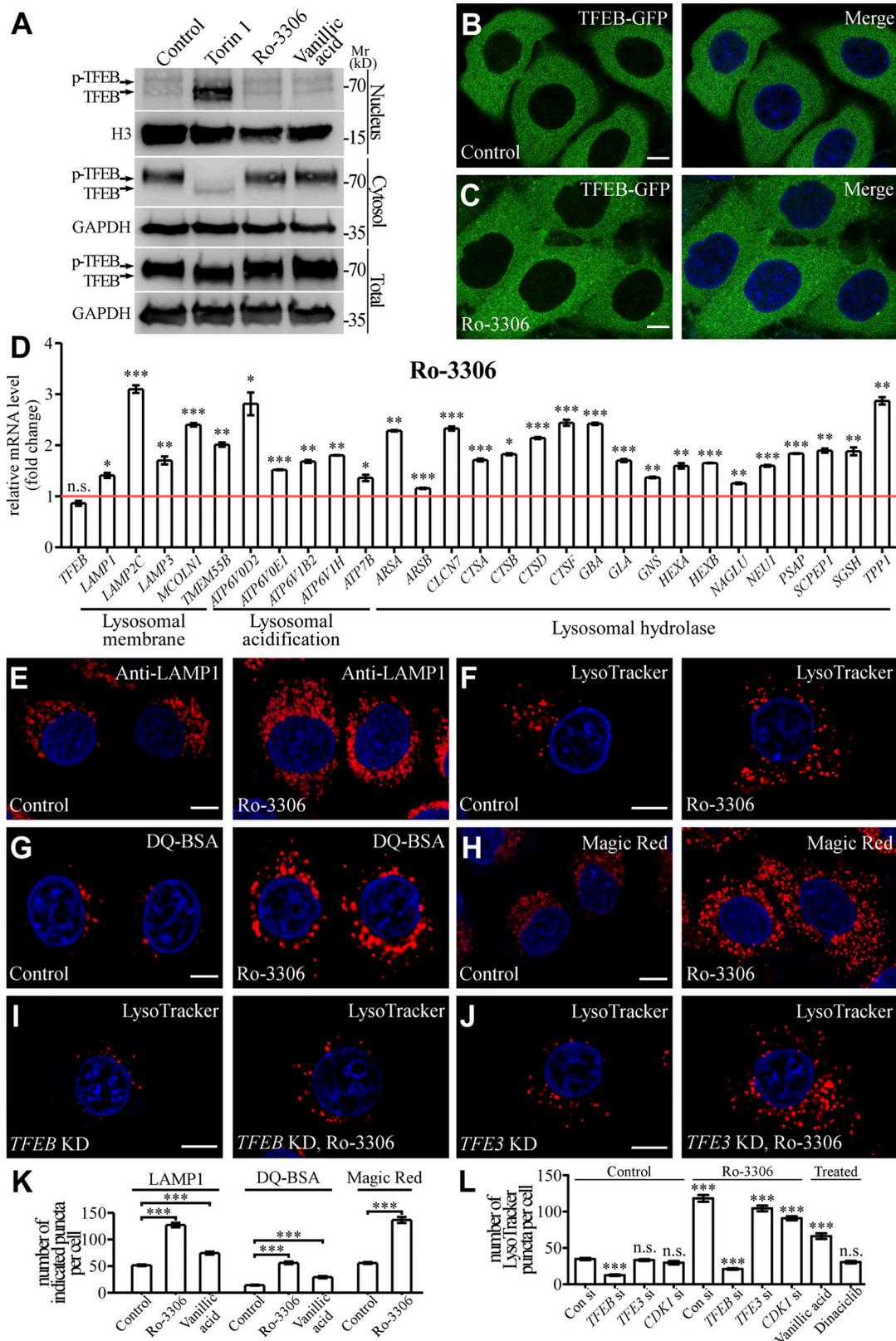
Figure 5. **Ro-3306 promotes lysosomal function and biogenesis in a TFEB-dependent manner. (A)** Western blotting assays showing the cytosolic and nuclear levels of endogenous TFEB. Treatment with 10 μM Ro-3306 or vanillic acid does not affect the levels, while 3-h Torin 1 treatment decreases the cytosolic level and increases the nuclear level. Phosphorylation of TFEB in whole-cell lysates, shown by the band shift, is affected by Torin 1, but not Ro-3306 or vanillic acid treatment. **(B and C)** In HeLa cells stably expressing TFEB-GFP, TFEB-GFP is predominantly localized in the cytoplasm (B). Treatment with 10 μM Ro-3306 (C) causes no change in the distribution of TFEB-GFP in HeLa cells. The nuclei of HeLa cells were stained by DAPI (blue channel) in B and C. **(D)** qRT-

PCR assays showing upregulation of mRNA levels of lysosomal genes in HeLa cells treated with 20 µM Ro-3306 for 24 h. The level of the corresponding mRNA in control cells is set to 1.0. Data (normalized by *GAPDH* level) are shown as mean ± SEM ($n = 3$ for each bar). *, $P < 0.05$; **, $P < 0.01$; *** $P < 0.001$. **(E–H)** Compared with control cells, more lysosomal structures are labeled by anti-LAMP1 antibody (E) or stained by LysoTracker (F), DQ-BSA (G), and Magic Red (H) in HeLa cells treated with 10 µM Ro-3306. Lysosomes labeled by these markers are more scattered in Ro-3306–treated cells than in control cells. **(I and J)** In HeLa cells treated with 10 µM Ro-3306, the increased number of lysosomes stained by LysoTracker (shown in F) is suppressed by simultaneous depletion of TFEB (I) but is not affected by TFE3 depletion (J). **(K)** Quantification of the number of LAMP1, DQ-BSA, and Magic Red puncta in control cells and cells treated with 10 µM Ro-3306 or vanillic acid. Data are shown as mean ± SEM ($n = 30, 30, 20, 30, 30, 30, 30$, and 30 cells for the treatments shown on the x axis). ***, $P < 0.001$. **(L)** Quantification of the number of LysoTracker-stained puncta in control cells and cells treated with 10 µM Ro-3306 or Dinaciclib with or without knockdown of TFEB, TFE3, or CDK1. Data are shown as mean ± SEM ($n = 30$ cells for each bar). ***, $P < 0.001$. All measured values were statistically compared with the first dataset. Scale bars: 10 µm (B, C, and E–J). Source data are available for this figure: SourceDataF5.

CDK1, was required for autophagy activation by Ro-3306 (Fig. 6, B–D; and Fig. S5, G and H).

Autophagy involves the formation of isolation membranes and their expansion to autophagosomes (Mizushima et al., 2011; Nakatogawa, 2020). Autophagosomes then undergo maturation and eventually form autolysosomes (Zhao and Zhang, 2019; Zhao et al., 2021). Compared with control cells, early autophagic structures, including puncta formed by endogenous ATG13 and WIPI2, were more abundant in Ro-3306–treated cells (Fig. 6, F–H; and Fig. S5, I and J). The tandem GFP-RFP-LC3 reporter was used to monitor autophagosome maturation (Kimura et al., 2007). As the GFP signal is quenched in acidic conditions, the RFP-positive and GFP-negative (RFP⁺GFP⁻) puncta represent acidified autolysosomes. In Ro-3306–treated HeLa cells, the percentage of RFP⁺GFP⁻ LC3 puncta among total LC3 puncta was dramatically increased both under normal conditions and after Torin 1 treatment (Fig. 6, I–K; and Fig. S5, K and L), suggesting that autophagosome maturation was also facilitated by Ro-3306 treatment. Transmission EM (TEM) imaging showed that the numbers of autophagic structures, including autophagosomes, amphisomes, autolysosomes, and lysosomes, were significantly increased in Ro-3306–treated cells (Fig. 6, L–N; and Fig. S5, M and N). Thus, Ro-3306 treatment facilitates multiple steps of the autophagy-lysosome pathway.

Ro-3306 promotes autophagic clearance of protein aggregates

We next investigated whether the elevated autophagy activity induced by Ro-3306 treatment degrades disease-related protein aggregates. A polyglutamine-expanded exon 1 fragment of the huntingtin protein (Htt97Q) forms aggregates that are degraded by autophagy (Rubinsztein et al., 2005). Compared with control cells, the number of Htt97Q-GFP aggregates and the protein level of Htt97Q-GFP were greatly decreased upon Ro-3306 treatment (Fig. 7, A–E). EPG5 is required for formation of degradative autolysosomes (Wang et al., 2016), and its loss of function causes the multisystem disorder Vici syndrome, which involves neurodegenerative symptoms (Cullup et al., 2013). The accumulation of LC3-labeled autophagic structures and p62 aggregates caused by *EPG5* depletion can be suppressed by enhancing autolysosome formation/degradation (Guo et al., 2014; Wang et al., 2016; Chen et al., 2020). Treatment with Ro-3306 dramatically reduced the accumulation of LC3-II and p62 in *EPG5*-depleted cells (Fig. 7, F–J). These results indicate that Ro-3306 promotes autophagic clearance of toxic protein aggregates and also suppresses the autophagy defect caused by impaired autophagosome maturation.

Discussion

Material properties govern the unique behaviors of TFEB condensates

TFEB condensates display some liquid-like properties, including high internal dynamics, spherical shape, and dissolution by 1,6-hexanediol (Chen et al., 2020). However, fusion of TFEB condensates is rarely detected in in vitro LLPS systems or in living cells. The stability of individual droplets during collision is specified by the rigidity of the interfacial film, which in turn is determined by the surface viscosity and elasticity (see Materials and methods for detailed theory; Biswas and Haydon, 1963; Tadros, 2013). For liquid-like protein or protein/RNA condensates with high fusion propensity (e.g., P granules and nucleoli), the interfacial tension or viscosity can be calculated by analyzing the fusion of two droplets (Brangwynne et al., 2009; Brangwynne et al., 2011; Elbaum-Garfinkle et al., 2015; Zhang et al., 2015; Feric et al., 2016). The time for two fusing droplets to assume a spherical shape, τ, is given by $\tau \approx \ell(\eta/\gamma)$, where η is the droplet viscosity, γ is the interfacial tension, and ℓ is the characteristic length scale (size of droplets). The interfacial tension can also be determined by measuring the shape of the flattening droplet by a prism (Feric et al., 2016).

Some of the techniques used for characterizing readily fusing liquid-like droplets are not suitable for analyzing protein condensates with low fusion propensity. A microrheology technique using the translational motion of probe particles has been adapted to determine the diffusion coefficient, D, which can then be used to determine the droplet viscosity (Elbaum-Garfinkle et al., 2015; Zhang et al., 2015; Feric et al., 2016). The translational motions of probe particles are impacted by the heterogeneous organization of proteins in the droplets. Here we developed or adapted several techniques (optical tweezers, the MPA technique, AuNR tracking assay, and AFM) to directly measure the fusion process and characterize the material properties of TFEB condensates, including interfacial tension, elasticity, and viscosity. For a specific protein condensate, the exact result for each property may vary when measured by different methods/techniques owing to the different physical principles and/or systemic errors. Thus, when comparing different condensates, it is important to measure the material properties by the same methods. By using the AuNR tracking assay, which allows us to probe both translational and rotational motions, we demonstrated that protein condensates have distinct viscosities on the surface and in the interior, which indicates that they possess an interfacial boundary. Compared with readily fusing PGL-3 condensates, the surface and interior
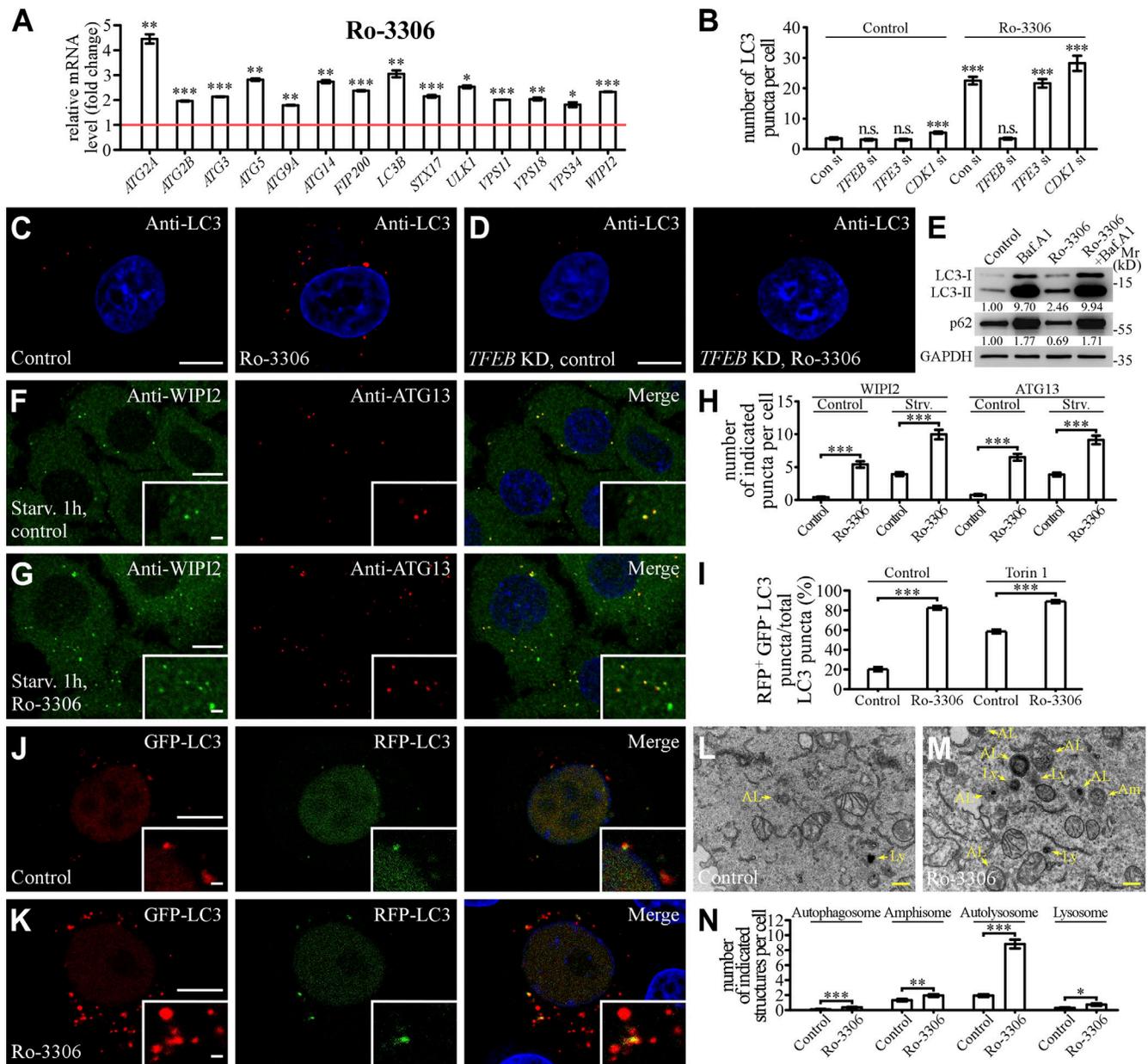
Figure 6. **Ro-3306 promotes autophagy activity. (A)** qRT-PCR assays showing upregulation of mRNA levels of autophagic genes in HeLa cells treated with 20 μM Ro-3306 for 24 h. The level of the corresponding mRNA in control cells is set to 1.0. Data (normalized by *GAPDH* level) are shown as mean ± SEM (*n* = 3 for each bar). *, P < 0.05; **, P < 0.01; *** P < 0.001. **(B–D)** The number of LC3 puncta stained by anti-LC3 antibody is increased in HeLa cells treated with 10 μM Ro-3306 (C), and this increase is suppressed by simultaneous depletion of TFEB (D). Quantification of the number of LC3 puncta per cell in control and Ro-3306–treated cells (B). Data are shown as mean ± SEM (*n* = 30 cells for each bar). ***, P < 0.001. All measured values were statistically compared with the first dataset. **(E)** Immunoblotting assays to determine the protein levels of LC3 and p62 in control and 10 μM Ro-3306–treated HeLa cells. Quantifications of LC3-II and p62 levels (normalized by GAPDH level) are shown. **(F–H)** Compared with control cells (F), the number of endogenous WIPI2 and ATG13 puncta stained by anti-WIPI2 and anti-ATG13 antibodies is higher in 10 μM Ro-3306–treated HeLa cells (G) after 1-h starvation. Quantification of the number of WIPI2 and ATG13 puncta per cell in control and Ro-3306–treated cells (H). Data are shown as mean ± SEM (*n* = 30 cells for each bar). ***, P < 0.001. **(I–K)** The RFP-GFP-LC3 assay in control and 10 μM Ro-3306–treated HeLa cells. Compared with control cells (J), more red-only puncta are formed in Ro-3306–treated cells (K) under normal conditions. Quantification of the percentage of RFP⁺GFP⁻ LC3 puncta among total LC3 puncta in control and Ro-3306–treated cells (I). Data are shown as mean ± SEM (*n* = 30, 29, 30, and 30 cells for control and Ro-3306 treatment under normal and Torin 1–treated conditions, respectively). ***, P < 0.001. **(L–N)** TEM images showing that the number of autophagic structures (autophagosomes and amphisomes) and lysosomal structures (autolysosomes and lysosomes) is increased in 10 μM Ro-3306–treated HeLa cells (M) compared with control cells (L). Quantifications of the number of autophagosomes, amphisomes, autolysosomes, and lysosomes in control and Ro-3306–treated cells are shown in N. Data are shown as mean ± SEM in N. (*n* = 94 cells for each bar). *, P < 0.05; **, P < 0.01; ***, P < 0.001. AL, autolysosome; Am, amphisome; Av, autophagosome; Ly, lysosome. Scale bars: 10 μm (C, D, F, G, J, and K); 1 μm (insets in F, G, J, and K); 500 nm (L and M). Source data are available for this figure: SourceDataF6.
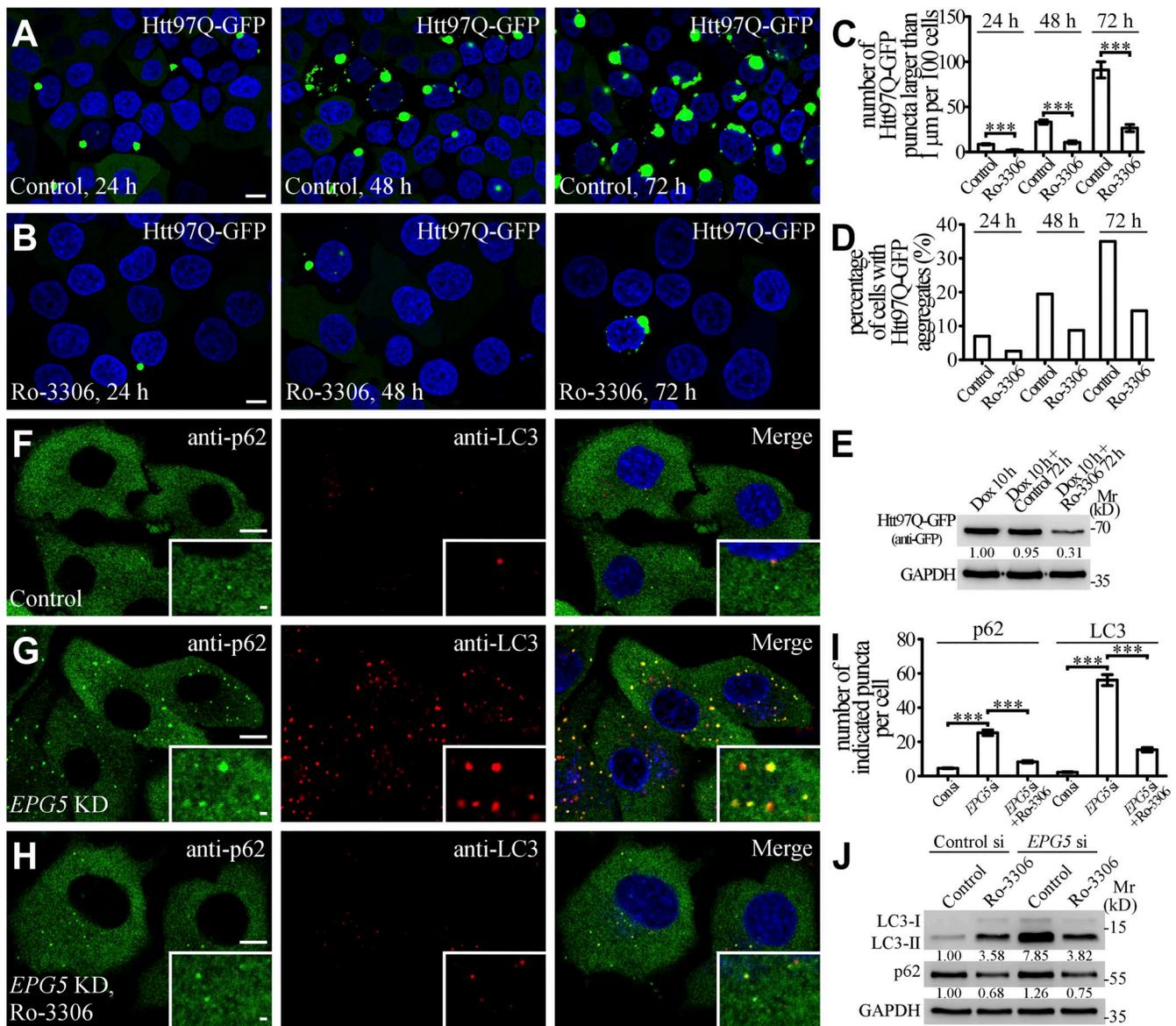
Figure 7. **Ro-3306 promotes autophagic clearance of toxic protein aggregates. (A–D)** HeLa cells stably expressing tet-on Htt97Q-GFP were incubated with 1 µg/ml doxycycline for 10 h. After the doxycycline was washed out, Htt97Q-GFP gradually assembled into protein aggregates in the cytosol with time (A). In cells incubated with 10 µM Ro-3306, the number of Htt97Q-GFP aggregates is dramatically reduced (B). Quantification at different time points of the number of Htt97Q-GFP puncta larger than 1 µm per 100 cells (C) and the percentage of cells with Htt97Q-GFP puncta (>300 cells from at least three independent experiments; D) in control and Ro-3306–treated cells, respectively. Data are shown as mean ± SEM in C (n > 300 cells from at least three independent experiments). ***, P < 0.001. **(E)** Immunoblotting assays showing the protein levels of Htt97Q-GFP in control and 10 µM Ro-3306–treated HeLa cells under normal condition. Quantifications of Htt97Q-GFP level (normalized by GAPDH level) are shown underneath. **(F–I)** Compared with control HeLa cells (F), the number of p62 and LC3 puncta stained by anti-p62 and anti-LC3 antibodies is increased in EPG5 KD cells (G). 10 µM Ro-3306 treatment inhibits the accumulation of p62 and LC3 puncta in EPG5 KD cells (H). Quantification of the number of p62 and LC3 puncta per cell for F–H (I). Data are shown as mean ± SEM (n = 30 cells for each bar). ***, P < 0.001. **(J)** Levels of LC3-II and p62 in control and EPG5 KD HeLa cells under normal and 10 µM Ro-3306–treated conditions are shown in immunoblotting assays. Quantifications of LC3-II and p62 levels (normalized by GAPDH level) are shown underneath. Scale bars: 10 µm (A, B, and F–H); 1 µm (insets in F–H). Source data are available for this figure: SourceDataF7.

viscosities of TFEB condensates are much higher, and the difference between the surface and interior is much larger. TFEB droplets also exhibit much higher elasticity than PGL-3 droplets. Mutating the positively charged residues in TFEB decreases the interfacial tension, the surface viscosity, and the elasticity, and hence enhances the fusion propensity. The thickness of the interfacial films is another important factor that determines

droplet stability (Biswas and Haydon, 1963). To date, no techniques have been developed to characterize the thickness of the interfacial boundaries of protein condensates. Our results indicate that different material properties govern the distinct interactions of different droplets, and liquid-like condensates may use the rigidity of interfacial boundaries to control their fusion propensity (Fig. 8 A).
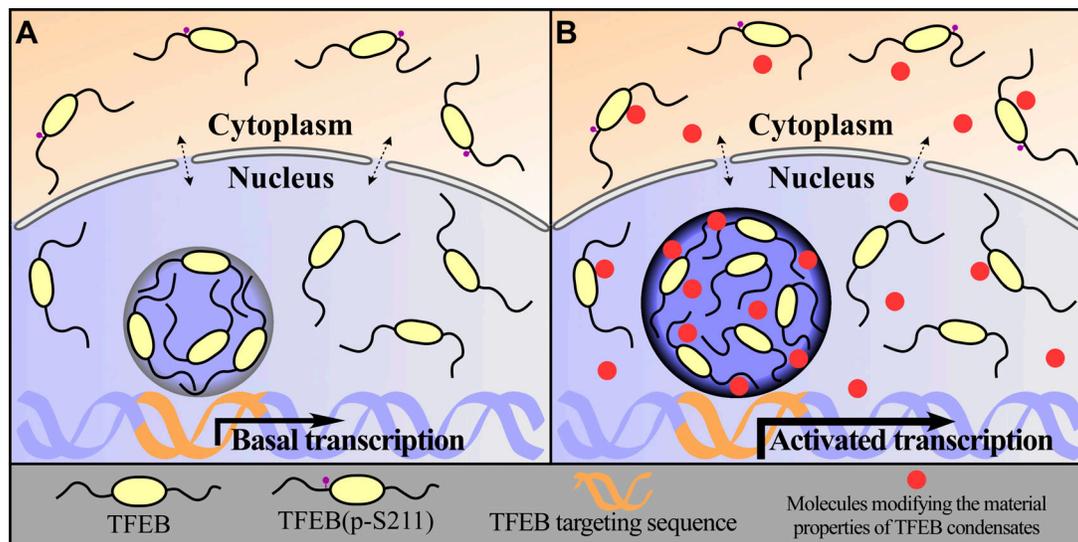
Figure 8. **Model showing that modifying the properties of TFEB condensates regulates the autophagy-lysosome pathway. (A and B)** The material properties of TFEB condensates, which govern their size and transcriptional activity, regulate the autophagy-lysosome pathway. Highly rigid interfacial boundaries on the surface of TFEB condensates determine their unique biophysical properties (A). Small molecules modifying the material properties of TFEB condensates modulate their transcription activity without altering the cytoplasmic-nuclear transport of TFEB (B).

Compared with TFEB, the TFEB(bHLH-B8A) mutant shows decreased ability to undergo LLPS in a buffer containing 200 mM NaCl in the in vitro LLPS system but exhibits higher fusion propensity in a buffer containing higher salt concentration, resulting in formation of larger condensates (Fig. 1, I, K, and L). TFEB(bHLH-B8A) also forms much larger condensates in the nucleus of living cells (Fig. 2, F and G). TFEB fails to phase separate in the cytoplasm but forms numerous condensates in the nucleus (Fig. S1, N and O). These results suggest that the nuclear environment, which is enriched in high-valency positively charged molecules such as Mg^{2+} and spermines, may mimic the high ionic strength in high-salt buffer in vitro.

Modulation of the material properties of TFEB condensates by small molecular compounds

Based on the size of TFEB droplets, we identified Ro-3306 and vanillic acid as modulators of the material properties of TFEB condensates and consequently of the fusion propensity of TFEB condensates. The phase state of TFEB condensates appears to become stable shortly after LLPS induction. However, Ro-3306 and vanillic acid dramatically slow down the phase transition of TFEB condensates. Within ~30 min after LLPS induction, interfacial tension and viscosities both on the surface and in the interior of TFEB/Ro-3306 and TFEB/vanillic acid condensates are lower than for TFEB condensates. Approximately 30 min after LLPS induction, the fusion propensity of TFEB/Ro-3306 and TFEB/vanillic acid condensates significantly decreases, and their interfacial tension and surface/interior viscosities dramatically increase and are even higher than those of TFEB condensates. The fusion and transition processes of TFEB condensates in living cells are too transient to be characterized. Compared with TFEB condensates in control cells, TFEB condensates in Ro-3306– and vanillic acid–treated cells are larger in size and show a decreased internal mobility, resembling the

aged droplets in in vitro LLPS systems. Ro-3306 and vanillic acid fail to change the behaviors of TFE3 condensates, indicating that their effect on protein LLPS is specific.

Ro-3306 is an ATP-competitive inhibitor that is presumed to directly occupy the ATP-binding pocket of CDK1. It strongly inhibits the catalytic activity of CDK1/cyclin B1 complex with an inhibitory constant, K_i, of 35 nM (Vassilev et al., 2006). We failed to detect evident binding between TFEB and Ro-3306 in isothermal titration calorimetry assays (not depicted), which suggests that their binding affinity is weak. Alternatively, assembly of TFEB condensates may create specific binding sites for Ro-3306. It remains to be determined whether Ro-3306 or vanillic acid is specifically enriched in TFEB condensates. The molecular mechanisms whereby these compounds modulate the material properties of TFEB condensates also await future investigation. Currently, it is still challenging to measure the dynamic weak interactions during LLPS of protein condensates. Strategies for designing and screening small molecules that inhibit protein LLPS have been used to regulate relevant biological processes and also to potentially intervene in disease (Fang et al., 2019; Wheeler et al., 2019; Zhou et al., 2020; Zhu et al., 2020). We demonstrated here that the material properties of protein condensates can also be modulated to alter their activities.

Modulation of the material properties of TFEB condensates regulates the autophagy-lysosome pathway

Ro-3306 and vanillic acid upregulate the transcriptional activity of TFEB condensates by modifying their material properties, but without altering nuclear-cytoplasmic trafficking (Fig. 8, A and B). Ro-3306/vanillic acid treatment further increases the number of lysosomes in Torin-1–treated cells, indicating that nuclear-cytoplasmic trafficking and modulation of material properties act additively or synergistically. The molecular mechanism whereby the material properties of TFEB

condensates govern their transcriptional activity has yet to be determined. High levels of transcribed RNA have been shown to dissolve transcriptional condensates to terminate transcription (Henninger et al., 2021). Compared with TFEB, TFEB/Ro-3306 and TFEB/vanillic acid form harder condensates, and it may be more difficult for transcribed RNA to dissolve them, resulting in their persistent involvement in gene transcription. Alternatively, the material properties of transcriptional condensates may directly modulate gene transcription.

Enhancement of lysosomal biogenesis and function by the identified compounds also elevates starvation-induced autophagy activity, increases selective autophagic degradation of protein aggregates formed by misfolded proteins and polyQ, and suppresses the autophagy defect caused by impaired autophagosome maturation. Increasing TFEB activity in neurodegenerative primary neurons and animal models has been proven to be effective in ameliorating the pathogenesis of various diseases associated with impaired lysosomal degradation, including Alzheimer's disease, Parkinson's disease, Huntington's disease, X-linked spinal and bulbar muscular atrophy, and lysosomal storage diseases (Decressac et al., 2013; Cortes et al., 2014; Raben and Puertollano, 2016; Li et al., 2016; Martini-Stoica et al., 2016; Song et al., 2021). Current approaches to activate TFEB are based on increasing its nuclear level via virus-mediated TFEB overexpression or modulating the activity of upstream kinases and phosphatases (Song et al., 2021). However, the targeted kinases (for example, mTORC1) also act in other essential pathways, and modulation of their activities has detrimental effects on cellular functions. Our study indicates that modifying the material properties of TFEB condensates provides a novel potential therapeutic strategy for the treatment of lysosome-associated diseases.

Materials and methods
Cell lines and reagents
HeLa cells stably expressing TFEB-GFP were kindly given by Dr. Richard Youle (National Institute of Neurological Disorders and Stroke, Bethesda, MD). HeLa cells stably expressing Tet-on Htt97Q-GFP were kindly given by Dr. Chonglin Yang (Yunnan University, Yunnan, China). HeLa and COS-7 cells were cultured in DMEM (SH30022.01B; Hyclone) with 10% FBS (SH30084.03; Hyclone) supplemented with penicillin-streptomycin at 37°C and 5% CO_2. For Torin 1 (14379; Cell Signaling Technology) treatment, cells were incubated with 1 µM Torin 1 at 37°C for 3 h. For Ro-3306 (T2356; TargetMol), vanillic acid (T9115; TargetMol), or Dinaciclib (779353-01-4; TargetMol) treatment, cells were incubated with 10 µM of each compound at 37°C for 24 h unless otherwise specified. For Gly-Phe-β-naphthylamide (GPN; K-1325.0250; Bachem) treatment, cells were incubated with 100 µM GPN at 37°C for 1 h. Transfection of plasmids was performed using Lipofectamine 2000 (11668019; Invitrogen). For the Magic Red CTSB and DQ-BSA assays, cells were incubated with Magic Red (937; Immunochemistry) and DQ-BSA (D12051, Invitrogen) according to the manufacturer's instructions for 1 and 24 h, respectively. For LysoTracker staining, cells were incubated with 0.5 µM LysoTracker (L7528; Life Technologies) at 37°C for 30 min before fixation. To inhibit autophagy activity,

cells were incubated with 30 nM Bafilomycin A1 (19-148; Millipore) at 37°C for 24 h.

Antibodies
Antibodies used were rabbit anti-TFEB (4240S; Cell Signaling Technology), mouse anti-LAMP1 (555798; BD Biosciences), mouse anti-LC3 (M152-3; MBL), rabbit anti-p62 (PM045; MBL), mouse anti-WIPI2 (ab105459; Abcam), rabbit anti-ATG13 (13468S; Cell Signaling Technology), goat anti-CTSD (sc-6486; Santa Cruz), mouse anti-GAPDH (B1034; Biodragon), and rabbit anti-p(Ser10)-H3 (NB21-1091; Novus Biologicals).

Plasmid construction
TFEB-GFP was kindly provided by Dr. Chonglin Yang. For construction of TFEB-GFP-NLS, a classic NLS (PKKKRKV) was inserted into the C terminus of TFEB-GFP. Other genes in this study were PCR-amplified from cDNA libraries, inserted into the indicated vectors, and confirmed by sequencing. TFE3 and GAL3 were cloned into pEGFP-C1, and PGL-3 was cloned into pEGFP-N1. The series of plasmids carrying point mutations of TFEB was generated by site-directed mutagenesis. The following primers were used for plasmid construction: TFEB-GFP-NLS forward, 5'-GAAGAAGAAGCGGAAGGTCTAAAGCGGCCGCGACTC-3'; reverse, 5'-CCTTCCGCTTCTTCTTCGGCTTGTACAGCTCGTCC-3'; GFP-TFE3 forward, 5'-TCCGGACTCAGATCTCGAATGTCTCATGCGGCCGAACC-3'; reverse, 5'-TTCGAAGCTTGAGCTCGATCAGGACTCCTCTTCCATGCTG-3'; PGL-3-GFP forward, 5'-TCCGGACTCAGATCTCGAATGGAAGCAAACAAACGAC-3'; reverse, 5'-TTCGAAGCTTGAGCTCGATTAGGAACCTCCACGGGATC-3'; MBP-TFEB forward, 5'-GTTCCAGGGGCCCGGATCCATGGCGTCACGCATAGGG-3'; reverse, 5'-GGAGCTCGAATTCGGATCACAGCACATCGCCCTCCTCC-3'; MBP-TFE3 forward, 5'-GTTCCAGGGGCCCGGATCCATGTCTCATGCGGCCGAACC-3'; reverse, 5'-GGAGCTCGAATTCGGATCAGGACTCCTCTTCCATGCTG-3'; TFEB(del bHLH) forward, 5'-GGGGATCGGGTTCCCAGAAGGACCTGCAAAAGTCCAG-3'; reverse, 5'-CTGGGAACCCGATCCCCGCTCCTTGGCCAGGGCCC-3'; TFEB(S211A) forward, 5'-GCAGCGCCTGCCCTGCGGACCTGACCCAG-3'; reverse, 5'-GGGCAGGCGCTGCTGGTGACGCCCACCAG-3'; TFEB(S142A) forward, 5'-CCCAATGCCCCCATGGCCATGCTGCACATTGG-3'; reverse, 5'-CATGGGGGCATTGGGAGCACTGTTGCCAGCGG-3'; TFEB(B2A) forward, 5'-CACAACTTAATTGAAAGGAGAGCAAGGTTCAACATCAATGACCGC-3'; reverse, 5'-CCTTTCAATTAAGTTGTGATTGTCTGCCTTCTGCCGCTCCTTGGC-3'; TFEB(B4A) forward, 5'-CATTGATGTTGAACCTTGCTCTCCTTTCAATTAAGTTGTGATTGTCTGCCTTCTGCCGCTCCTTGGC-3'; reverse, 5'-GGTTCAACATCAATGACCGCATCGCGGAGTTGGGAATGCTGATCCCCGCGGCCAATGACCTGGACGTG-3'; TFEB(B4A-B6A) forward, 5'-CTCAAGGCCTCTGTGGATTACATCGCGAGGATGCAGAAGGACC-3'; reverse, 5'-CACAGAGGCCTTGAGGATGGTGCCCGCGTTCCAGCGCACGTCC-3'; and TFEB(B4A-B8A) forward, 5'-CCATCCTCGCGGCCTCTGTGGATTACATCGCGAGGATGCAGAAGGAC-3'; reverse, 5'-GGCCGCGAGGATGGTGCCCGCGTTCCAGGCCACGTCCAGGTCATTG-3'.

RNA interference
Cells were transfected with control and siRNAs targeting the indicated genes with Lipofectamine RNAiMAX (13778150;

Wang et al.
Material properties of TFEB condensates

Journal of Cell Biology   15 of 21
https://doi.org/10.1083/jcb.202112024

Invitrogen), cultured at 37°C for 48 h, and treated with Ro-3306 or vanillic acid for another 24 h. Double-stranded siRNAs were ordered from GenePharma. siRNAs used in this study are as follows: Control: 5′-UUCUCCGAACGUGUCACGUTT-3′; hTFEB-1: 5′-UGUAAUGCAUGACAGCCUGTT-3′; hTFEB-2: 5′-AUUGUC UUUCUUCUGCCGCTT-3′; hTFEB-3: 5′-UUGAUGUUGAACCUU CGUCTT-3′; hTFE3-1: 5′-AUCCCUGCUCUCUUCAGUGTT-3′; hTFE3-2: 5′-AGGGCUGCUUUCCUUGGCCTT-3′; hTFE3-3: 5′-UCA UCAGCCUGGAGUCCAGTT-3′; hCDK1-1: 5′-CCUAUGGAGUUG UGUAUAATT-3′; hCDK1-2: 5′-GGUCAGUACAUGGAUUCUUTT-3′; hCDK1-3: 5′-GGAUGUGCUUAUGCAGGAUTT-3′; and hEPG5: 5′-GAACAGGUGUACCCAAGCUTT-3′.

Immunostaining assays
Cells cultured on coverslips were washed three times with PBS, fixed with 4% PFA for 20 min, and permeabilized for 10 min at RT with 100 µg/ml Digitonin (D141; Sigma-Aldrich) for permeabilization of the plasma membrane or 5‰ Triton X-100 for permeabilization of the nuclear membrane. Cells were blocked with 5% goat serum for 60 min and then incubated with the indicated primary antibodies overnight at 4°C. After three washes with PBS, cells were stained with fluorescently labeled secondary antibodies for 1 h at RT and observed using a confocal microscope (LSM 880 Meta plus Zeiss Axiovert Zoom; Zeiss) equipped with a 63×/1.40 oil-immersion objective lens (Plan-Apochromat; Zeiss) and a camera (AxioCam HRm; Zeiss) at RT.

Immunoblotting assays
Cells were washed with PBS three times and lysed with 2× SDS loading buffer (400 mM Tris-HCl, pH 6.8, 0.04 g/ml SDS, 20% glycerol, and 0.056 g/ml DTT), boiled at 100°C for 10 min, subjected to SDS-PAGE, and transferred to a polyvinylidene difluoride (PVDF) membrane. The PVDF membrane was incubated with corresponding primary and secondary antibodies and exposed on an imaging system (ChemiScope 6000 Touch; ClinX). The acquired images were further processed with Adobe Photoshop CS6 and analyzed with ImageJ.

Live-cell imaging
Cells were cultured on glass-bottom dishes (801001; NEST) and transfected with the indicated plasmids. 24 h after transfection, cells were treated with 1 µM Torin 1 and imaged at 37°C with 5% CO_2 using a 100×/1.45 oil-immersion objective lens (CFI Plan Apochromat Lambda; Nikon) on an inverted fluorescence microscope (Eclipse Ti-E; Nikon) with a spinning disk confocal scanner uniter (UltraView; PerkinElmer). For Ro-3306 or vanillic acid treatment, cells were incubated with 10 µM Ro-3306 or vanillic acid 20 h after transfection at 37°C for another 23 h and coincubated with 1 µM Torin 1 for 1 h before imaging. Time-lapse images were acquired every 20 or 30 s for a total of 30 min or 1 h and analyzed with Volocity software (PerkinElmer).

Quantitative real-time PCR (qRT-PCR) assays
Total RNAs were extracted from HeLa cells with Trizol (15596018; Life Technologies) and reverse transcribed into cDNA using a RevertAid First Strand cDNA Synthesis Kit (K1622; Thermo Fisher Scientific). qRT-PCR of the indicated cDNA was conducted using UltraSYBR Mixture (High ROX; CW2602M, CWBIO) on a QuantStudio 7 Flex (Applied Biosystems) instrument. For Ro-3306 or vanillic acid treatment, cells were incubated with 20 µM Ro-3306 or vanillic acid at 37°C for 24 h. The sequences of primers used for qRT-PCR experiments were as follows: LAMP1 forward, 5′-ACGTTACAGCGTCCAGCTCAT-3′; reverse, 5′-TCTTTGGAGCTCGGCATTGG-3′; LAMP2C forward, 5′-GTATTCTACAGCTGAAGAATGTTCTG-3′; reverse, 5′-ACACCC ACTGCAACAGGAAT-3′; LAMP3 forward, 5′-AGGTTCTAAACG GAAGC-3′; reverse, 5′-AGACGGTCAAATAGGC-3′; MCOLN1 forward, 5′-TTGCTCTCTGCCAGCGGTACTA-3′; reverse, 5′-GCA GTCAGTAACCACCATCGGA-3′; TMEM55B forward, 5′-GTTCGA TGCCCCTGTAACTGTC-3′; reverse, 5′-CCCAGGTTGATGATT CTTTTGC-3′; ATP6V0D2 forward, 5′-CATTCTTGAGTTTGAGGC CG-3′; reverse, 5′-CCGTAATGATCCGCTACGTT-3′; ATP6V0E1 forward, 5′-CATTGTGATGAGCGTGTTCTGG-3′; reverse, 5′-AAC TCCCCGGTTAGGACCCTTA-3′; ATP6V1B2 forward, 5′-GAGGGG CAGATCTATGTGGA-3′; reverse, 5′-GCATGATCCTTCCTGGTC AT-3′; ATP6V1H forward, 5′-GGAAGTGTCAGATGATCCCCA-3′; reverse, 5′-CCGTTTGCCTCGTGGATAAT-3′; ATP7B forward, 5′-GTGGGCAATGACACCACTTT-3′; reverse, 5′-TGGGTGCCTTTG ACATCTGA-3′; ARSA forward, 5′-AGAGCTTTGCAGAGCGTT CAG-3′; reverse, 5′-ATACGCATGGTCTCAGGTCCA-3′; ARSB forward, 5′-ATCAGTGAAGGAAGCCCATCC-3′; reverse, 5′-ACA CGGTGAAGAGTCCACGAA-3′; CLCN7 forward, 5′-TGATCTCCA CGTTCACCCTGA-3′; reverse, 5′-TCTCCGAGTCAAACCTTCCGA-3′; CTSA forward, 5′-CAGGCTTTGGTCTTCTCTCCA-3′; reverse, 5′-TCACGCATTCCAGGTCTTTG-3′; CTSB forward, 5′-AGTGGA GAATGGCACACCCTA-3′; reverse, 5′-AAGAAGCCATTGTCACCC CA-3′; CTSD forward, 5′-AACTGCTGGACATCGCTTGCT-3′; reverse, 5′-CATTCTTCACGTAGGTGCTGGA-3′; CTSF forward, 5′-ACAGAGGAGGAGTTCCGCACTA-3′; reverse, 5′-GCTTGCTTC ATCTTGTTGCCA-3′; GALNS forward, 5′-TTGTCGGCAAGTGGC ATCT-3′; reverse, 5′-CCAAACCACTCATCAAATCCG-3′; GBA forward, 5′-TGGGTACCCGGATGATGTTA-3′; reverse, 5′-AGA TGCTGCTGCTCTCAACA-3′; GLA forward, 5′-AGCCAGATTCCT GCATCAGTG-3′; reverse, 5′-ATAACCTGCATCCTTCCAGCC-3′; GNS forward, 5′-CCCATTTTGAGAGGTGCCAGT-3′; reverse, 5′-TGACGTTACGGCCTTCTCCTT-3′; HEXA forward, 5′-CAACCA ACACATTCTTCTCCA-3′; reverse, 5′-CGCTATCGTGACCTGCTT TT-3′; HEXB forward, 5′-TCTGCTCCTTGGTACT-3′; reverse, 5′-CTGTCATAGGCGTCATC-3′; NAGLU forward, 5′-CAGAAGGAA GGAGCAGGAGT-3′; reverse, 5′-ATGTTCCCGAGGCTGTCAC-3′; NEU1 forward, 5′-CAGCACATCCAGAGTTCCGAGT-3′; reverse, 5′-TGTCTCTTTCCGCCATGAGGT-3′; PSAP forward, 5′-GCCAAC AGTGAAATCCCTTCC-3′; reverse, 5′-TCAGTGGCATTGTCCTTC AGC-3′; SCPEP1 forward, 5′-GATCTCCCCTGTTGATTCGGT-3′; reverse, 5′-AGCCCCTTATTTACGGCATTC-3′; SGSH forward, 5′-TGACCGGCCTTTCTTCCTCTA-3′; reverse, 5′-GCTCTCTCCGTT GCCAAACTT-3′; TPP1 forward, 5′-GATCCCAGCTCTCCTCAA TACG-3′; reverse, 5′-GCCATTTTGCACCGTGTG-3′; TFEB forward, 5′-CCAGAAGCGAGAGCTCACAGAT-3′; reverse, 5′-TGT GATTGTCTTTCTTCTGCCG-3′; TFE3 forward, 5′-GAGGCACCA CAGGACTGC-3′; reverse, 5′-TTGACTACTGTACACATCAAGCAG A-3′; CDK1 forward, 5′-ACAGGTCAAGTGGTAGCCATG-3′; reverse, 5′-CCATGTACTGACCAGGAGGG-3′; GAPDH forward, 5′-TGCACCACCAACTGCTTAGC-3′; reverse, 5′-GGCATGGACTGT

GGTCATGAG-3′; *ATG2A* forward, 5′-GCTCAGGGTACATGGAGC TG-3′; reverse, 5′-CTCGTGGTCTGTAAGGCTCAC-3′; *ATG2B* forward, 5′-AACTGCTGACGAATCCTCAGG-3′; reverse, 5′-GGGGTT CCAGCTAGGTGAGA-3′; *ATG3* forward, 5′-GACCCCGGTCCTCAA GGAA-3′; reverse, 5′-TGTAGCCCATTGCCATGTTGG-3′; *ATG5* forward, 5′-GAAGGAGGAGCCATAGCTTG-3′; reverse, 5′-CAT TTCAGTGGTGTGCCTTC-3′; *ATG9A* forward, 5′-CTGCCCTTC CGTATTGCAC-3′; reverse, 5′-CTCACGTTTGTGGATGCAGAT-3′; *ATG14* forward, 5′-GCGCCAAATGCGTTCAGAG-3′; reverse, 5′-AGTCGGCTTAACCTTTCCTTCT-3′; *FIP200* forward, 5′-ATCGAA GAGTGTGTACCTACAGT-3′; reverse, 5′-GCAGGTGGACGATCA CATAAGAT-3′; *LC3B* forward, 5′-GAGAAGACCTTCAAGCAG-3′; reverse, 5′-GAGGCATAGACCATGTACAG-3′; *STX17* forward, 5′-GCAGAATCTGGGACAAGTTG-3′; reverse, 5′-CTCTGAGAACTA GCTTCAGC-3′; *ULK1* forward, 5′-GGCAAGTTCGAGTTCTCCCG-3′; reverse, 5′-CGACCTCCAAATCGTGCTTCT-3′; *VPS11* forward, 5′-CGGCGCTTCGTTTTCTTCG-3′; reverse, 5′-CCCGTAGTTTGT AGGCTTGGAA-3′; *VPS18* forward, 5′-CACTCGGGGTATGTGAAT GCC-3′; reverse, 5′-TCGGAAGGGGTGAAGTCAATG-3′; and *WIPI2* forward, 5′-CCATCGTCAGCCTTAAAGCAC-3′; reverse, 5′-TCCAGGCATACTATCAGCCTC-3′.

Protein expression and purification
All genes were PCR-amplified and cloned into an in-house-modified version of pET-32a vector to produce N-terminal tandem MBP-His$_6$-tagged recombinant proteins. The MBP-His$_6$ tags were removed by protease 3C. Point mutations and truncations were generated by site-directed mutagenesis.

The recombinant proteins were expressed in *Escherichia coli* BL21-CodonPlus (DE3) strains. The *E. coli* cells carrying expression plasmids were cultured in LB medium at 37°C to OD$_{600}$ ≈ 0.6. To induce protein expression, 0.3 mM IPTG was added, and the cells were continuously cultured in an 18°C shaker at 220 rpm for 18 h. The bacterial cells were collected by sedimentation at 5,000 rpm for 15 min. For protein purification, the collected bacterial cells were resuspended in binding buffer (50 mM Tris-HCl, pH 7.9, 500 mM NaCl, and 10 mM imidazole), lysed with a high-pressure homogenizer, and sedimented at 18,000 rpm for 30 min at 4°C. The lysate supernatants were affinity purified with Ni-NTA agarose beads (30210; Qiagen). After extensive washes with binding buffer, the bound proteins were eluted with elution buffer (50 mM Tris-HCl, pH 7.9, 500 mM NaCl, and 500 mM imidazole). The eluted proteins were loaded onto desalting columns (17-0851-01; GE Healthcare), eluted with buffer containing 20 mM Hepes, pH 7.5, and 500 mM NaCl, concentrated, and stored in aliquots at –80°C. Protease 3C was purified by the same protocol mentioned above except that the buffer for elution from desalting columns contained 20 mM Hepes, pH 7.5, and 150 mM NaCl. For Cy3 labeling, TFEB was eluted from the Ni-NTA beads, mixed with 500 mM DTT and 50 µg/ml sulfo-cyanine3 maleimide (41380; Lumiprobe), and incubated for 1 h at 4°C.

In vitro phase separation assays
In vitro phase separation experiments were performed as described (Wang et al., 2019). All the proteins were centrifuged at 13,000 rpm for 10 min to remove undissolved protein aggregates before LLPS experiments. Buffers containing 20 mM Hepes, pH 7.5, and various concentrations of NaCl were used for LLPS. For protease-induced LLPS, 0.5 µl of 5 mg/ml protease 3C was added into each system to initiate phase separation. For LLPS of PGL-3, the purified protein was diluted with a buffer containing 20 mM Hepes, pH 7.5, to adjust the concentration of NaCl to 150 mM and the concentration of PGL-3 to 3 µM. After 2-min induction, each LLPS system was pipetted onto a glass slide and detected on an Imager M2 microscope (Zeiss) for differential interference contrast (DIC) imaging equipped with a 100×/1.40 oil DIC objective lens (Plan-Apochromat; Zeiss) and a camera (AxioCam MRm; Zeiss) at RT. For sedimentation assays, LLPS was induced in the system (volume 100 µl) for 5 min via cleavage of the MBP tag. After induction, centrifugation was carried out at 13,000 rpm for 5 min, and the supernatant and pellets were separated into two Eppendorf tubes and adjusted to equal volume with SDS loading buffer. The samples were boiled for 10–20 min and subjected to SDS-PAGE and Coomassie brilliant blue staining.

For examination of fusion events, LLPS systems were pipetted onto glass slides and detected under the DIC mode. Encounters between droplets were randomly detected and recorded. Cy3-labeled MBP-TFEB was also used for the time series experiments to examine droplet growth and fusion events. LLPS of TFEB(Cy3) was induced by adding 0.5 µl of 0.5 mg/ml protease 3C. Upon addition of protease, the system was immediately pipetted onto a glass-bottom cell culture dish for fluorescence imaging on a confocal microscope at RT. Images were taken continually for a total of ~11 min.

FRAP analysis
Droplets formed by Cy3-labeled MBP-TFEB protein were used for FRAP analysis. TFEB-GFP puncta in HeLa cells were used for the in vivo FRAP assay. The experiments were performed on a confocal microscope (LSM 880 Meta plus Zeiss Axiovert Zoom; Zeiss) equipped with a 63×/1.40 oil-immersion objective lens (Plan-Apochromat; Zeiss) and a camera (AxioCam HRm; Zeiss) at RT. The in vivo FRAP assays were performed at 37°C with 5% CO$_2$. Selected regions were photobleached at 561 nm for Cy3 and 488 nm for GFP, and the fluorescence intensities in these regions were collected every 2 s as mean region of interest. The value of signals was normalized to the initial intensity before photobleaching. Recovery curves were plotted using GraphPad Prism software.

Biswas and Haydon model for breakup of interfacial films
Fusion between two liquid droplets involves deformation and breakup of interfacial boundaries of the encountering droplets and mixing of their internal constituents. Quantitative description of the time for interfacial boundaries of encountering protein condensates to rupture, to our knowledge, is lacking. Biswas and Haydon (1963) deduced an equation to calculate the time for the breakup of interfacial films between a drop covered with a viscoelastic film and a plane viscoelastic film, which could serve as a reference for understanding the coalescence of protein condensates with viscoelastic properties. The equation is

$$\tau = \eta_s \left[3c' \frac{h^2}{A} - \frac{1}{G} - \Phi(t) \right],$$

where τ is the coalescence time, η_s is the interfacial viscosity, $3c'$ is a critical deformation factor describing the maximum indentation of the surfaces of the droplets where the interfacial films collapse, h is the thickness of the interfacial film, A is the Hamaker constant, G is the instantaneous elastic modulus, and $\Phi(t)$ is the retarded elastic deformation per unit stress. $\Phi(t)$ is negatively related to the elastic modulus. The instantaneous modulus G is a function of time that is positively related to the elastic modulus of the film. Therefore, the time τ required for the encountering droplets and films to coalesce under a certain stress is determined by the surface viscosity η_s, the thickness of the interfacial film h, and also the elastic modulus (Biswas and Haydon, 1963).

Optical tweezers experiments
Optical tweezers experiments were performed on liquid droplets using dual-beam mini-tweezers dual-trap optical tweezers (Smith et al., 1996). Newly induced TFEB droplets diluted with pre-prepared saturated protein solutions were used for the experiments. The droplets were ~5–10 μm in diameter. To prepare saturated protein solutions, 10 μM TFEB or 1 μM PGL-3 proteins were induced for LLPS in a buffer containing 500 or 150 mM NaCl, respectively, for 2 h at RT. The LLPS systems were centrifuged for 10 min at 13,000 rpm, and the supernatant was collected, filtered through a 0.22-μm membrane, and used as the saturated protein solution. Droplets newly induced with 80 μM MBP-TFEB or 12 μM PGL-3 protein in 500 or 150 mM NaCl buffer, respectively, were diluted with saturated protein solution. During the experiments, one droplet was trapped by the laser beams (with a constant stiffness of ~0.1 pN/nm), and another droplet was positioned by suction on the tip of a micropipette that was fixed in the chamber. The laser beams were coupled to a piezoelectric flexure stage that allows small displacements. The distance between the two droplets was controlled by moving the piezoelectric stage at 100 nm/s. A light-lever system was attached to the stage to record the positional changes of the laser-trapped droplet. During the experiments, the two droplets were pushed against each other and pulled away repeatedly. The displacement of the laser-trapped droplet was monitored, and the force between the droplets was calculated. All of the optical tweezers experiments were carried out at 23 ± 1°C.

Micropipette interfacial tension measurements
The interfacial tension γ of the droplets was measured on an optical microscope with the micromanipulation technique (Drelich et al., 2002). All coverslips and micropipettes used in the experiments were coated with PLL(20)-g(3,5)-PEG(2) (Xi'an ruixi Biological Technology Co.) to prevent droplet adsorption. Droplets newly induced with 80 μM MBP-TFEB or 12 μM PGL-3 proteins in a buffer containing 500 or 150 mM NaCl buffer diluted with saturated protein solution were pipetted onto the coated coverslip and observed with an optical microscope. The droplet diameter was ~5–10 μm. A single droplet was gripped by

a micropipette with negative pressure generated by a water tower and lifted from the coverslip. The negative pressure was adjusted so that the droplet was just drawn into the micropipette. Pictures of the droplets were taken at this stage and analyzed with ImageJ. The interfacial tension was calculated with the following equation:

$$\gamma = \frac{\Delta P}{2\left(1/R_P - 1/R_D\right)},$$

where ΔP, R_P and R_D represent the negative pressure generated by the water tower, the inner radius of the micropipette, and the radius of the droplet, respectively.

AuNR experiments
TFEB or PGL-3 droplets newly induced using 80 μM MBP-TFEB or 12 μM PGL-3 proteins with coaddition of AuNRs in a buffer containing 500 mM NaCl were diluted with saturated TFEB protein solution and used for the experiments. The AuNRs used in the experiments were coated with cetyltrimethylammonium bromide, and their size was ~40 × 80 nm as deduced from TEM images. Dark-field imaging of AuNRs was performed at RT on a Nikon 80i upright microscope with a 100-W halogen tungsten lamp, an oil-immersion dark-field condenser (NA 1.20~1.43), and a long-working-distance 40× objective (working distance = 2.8~3.6, NA = 0.6). The detector used was either a color CMOS camera (DP74; Olympus) or an ultrahigh-speed monochrome CMOS camera (HS4; Pco). To acquire the rotational behaviors of single AuNRs, a birefringent prism was placed in the detection path, which separated the X and Y polarized scattered light from the AuNRs (Forkey et al., 2000). For translational tracking of single AuNRs, the exposure time of the color DP74 camera was 17.4 ms, and the frame rate was 30 Hz. For rotational tracking of single AuNRs, the exposure time of the ultrahigh-speed HS4 camera was 500 μs, and the frame rate was 1,974 Hz.

The scattered light from AuNRs is split into two orthogonal polarization channels, I_x and I_y, and then captured by the camera. The rotational behavior of AuNRs is calculated by autocorrelation analysis of the polarization factor $P = (I_x - I_y)/(I_x + I_y)$. The autocorrelation decay curves can be fitted by the Kohlrausch-Williams-Watts equation $P(t) = P(0) \exp[-(t/\tau_{kww})^\beta]$, where $P(0)$ is the normalization constant, τ_{kww} is the characteristic time, and β is the stretching exponent. The mean correlation time is derived by $\tau = \tau_{kww}*\Gamma(1/\beta)/\beta$, where Γ is the Gamma function. The apparent rotational diffusion coefficient of the AuNRs is then calculated by $D_r = 1/(6\tau)$, and the apparent viscosity can be determined from the Tirado and Garcia de la Torre theory: $D_r = (3k_BT)/(\pi\eta L^3)(\ln L/d + \sigma)$, with $\sigma = -0.662 + 0.917d/L - 0.05d^2/L^2$. Here, k_B is the Boltzmann constant, T is the temperature, η is the fluid viscosity, L is the longitudinal length of the AuNRs, and d is the axial diameter of the AuNRs. To avoid other factors interfering with the determination of viscosity, the viscosity calculated from the translational motions of AuNRs in the exterior solution is used as an internal reference to calculate the viscosity inside the droplets (Sonnichsen and Alivisatos, 2005). Thus, the viscosity distribution across the LLPS droplet can be measured by the rotational dynamics of the AuNRs.

To acquire the tracks of the translational movements of the AuNRs, the time-lapse pictures were analyzed with ImageJ. The tracks of the AuNRs and the droplets were captured over time, and the tracks of the AuNRs were corrected by subtracting the tracks of the droplets.

AFM experiments

For mechanical measurements, we used an AFM instrument (MFP-3D; Asylum Research) equipped with a colloidal probe (spring constant $k \approx 0.6$ N/m, sphere diameter $d \approx 18$ μm). The surface of the probe was coated with a thin layer of PLL-g-PEG, which provided a high degree of resistance to protein adsorption in the solution and also reduced adhesion on the droplet surface (Shen et al., 2017). The AFM measurements were performed in the contact mode by moving the colloidal probe vertically on the top of the droplet, which had a diameter of ~5–10 μm. The z-axis piezoelectric actuator of the AFM was controlled to move the probe up or down at a constant speed of 10 μm/s. AFM measured the force generated by deformation of the condensed droplets after the probe compressed the droplets. When a target force (~2 nN) was reached, the AFM probe retracted. The approach curves obtained in this way were found to be well described by the Hertz model (Hertz, 1881), $F = \frac{4}{3}ER^{\frac{1}{2}}\delta^{\frac{3}{2}}$, where E is the reduced Young's modulus of the material, $R = 1/(1/R_1 + 1/R_2)$ is the effective radius of the probe $R_1 = d/2$ and the droplet R_2, and δ is the indentation depth.

High-throughput screening of small molecular compounds

High-throughput screening of small molecular compounds was performed on an Opera Phenix (PerkinElmer) high-content screening microscope in screening buffer containing 20 mM Hepes, pH 7.5, 500 mM NaCl, and 1% DMSO at 20°C. 5,770 small molecular compounds from the Bioactive Compound Library (L4000; TargetMol) and the Natural Compound Library (L6000; TargetMol) were screened in this study. Small molecular compounds dissolved in DMSO with a concentration of 10 mM were diluted with 20 mM Hepes, pH 7.5, and 500 mM NaCl to a final concentration of 100 μM, and the final buffer was the same as the screening buffer. 15 μM Cy5-labeled MBP-TFEB and 30 μM small molecules were mixed in CellCarrier-96 ultra (6055300; PerkinElmer) plates. 15 μM Cy5-labeled MBP-TFEB without small molecules was used as the negative control. Protease 3C in screening buffer was added to induce LLPS. The final volume was adjusted to 100 μl. The screening systems in CellCarrier-96 ultra plates were incubated at RT for 2 h and then imaged on Opera Phenix.

Subcellular fractionation

After three washes with PBS, HeLa cells were lysed with lysis buffer (20 mM Hepes, pH 7.5, 150 mM NaCl, 10% glycerol, 5 mM EDTA, and 0.5% Triton X-100) supplemented with protease inhibitor cocktail (B14003; Bimake) on ice for 20 min. The lysates were centrifuged at 13,000 rpm for 15 min at 4°C, and the supernatants were collected and mixed with an equal volume of 5× SDS loading buffer (1 M Tris-HCl, pH 6.8, 0.1 g/ml SDS, 50% glycerol, and 0.14 g/ml DTT), boiled, and used as the cytosolic fractions. The pellets were extensively washed with lysis buffer at least three times, subjected to sonication in 2× SDS loading buffer (400 mM Tris-HCl, pH 6.8, 0.04 g/ml SDS, 20% glycerol, and 0.056 g/ml DTT), boiled, and used as the nuclear fraction.

TEM

For TEM analysis, cells were fixed with 2.5% glutaraldehyde dissolved in PBS overnight at 4°C and postfixed with 1% OsO₄ and 1% potassium ferrocyanide for 90 min the next day. The cells were washed with ddH₂O and stained with 2% uranyl acetate for 1 h at RT. After washing with ddH₂O, the cells were further treated with a graded ethanol series (30, 50, 70, 80, 95, 100, 100, and 100% for 10 min each) for dehydration and penetrated with epoxy resin. The cells were embedded in epoxy resin and polymerized at 60°C for 48 h. Ultrathin sections were stained with lead citrate. Images were examined under a 120-kV electron microscope (H-7650B; Hitachi) at 100 kV with an AMT CCD camera (XR-41) using Digital Micrograph software at RT.

For DAB staining, cells were transfected with plasmids expressing GFP-APEX2 and GFP-APEX2-LC3. Monolayer cells were fixed with 2.5% glutaraldehyde dissolved in PBS overnight at 4°C and rinsed five times for 1 min in PBS on ice. The cells were then treated with 20 mM glycine for 5 min, followed by five rinses for 1 min in PBS. After treatment with a freshly diluted solution of 0.5 mg/ml (1.4 mM) DAB tetrahydrochloride for 10 min, the cells were rinsed five times for 1 min in chilled buffer. Then the cells were postfixed in 1% OsO₄ for 10 min on ice, rinsed five times for 1 min in ddH₂O, and placed in chilled 2% aqueous uranyl acetate for 30 min. After washing with ddH₂O, the cells were dehydrated with a graded series of ethanol solutions and embedded in epoxy resin.

Assays for measuring autophagic degradation of protein aggregates

For determining degradation of Puromycin-induced p62 aggregates, HeLa cells treated with DMSO or 10 μM Ro-3306 for 24 h were incubated with 5 μg/ml Puromycin for the indicated time. Cells were fixed, immunostained with anti-p62 antibody, and observed with confocal microscopy (LSM 880 Meta plus Zeiss Axiovert Zoom; Zeiss) equipped with a 63×/1.40 oil-immersion objective lens (Plan-Apochromat; Zeiss) and a camera (AxioCam HRm; Zeiss) at RT.

For examining degradation of Htt97Q-GFP aggregates, HeLa cells stably expressing Tet-on Htt97Q-GFP were incubated with 1 μg/ml doxycycline for 10 h to induce Htt97Q-GFP expression. Cells were washed three times with PBS buffer and incubated with DMSO or 10 μM Ro-3306 for the indicated times. Htt97Q-GFP foci were observed with a confocal microscope (LSM 880 Meta plus Zeiss Axiovert Zoom; Zeiss) equipped with a 63×/1.40 oil-immersion objective lens (Plan-Apochromat; Zeiss) and a camera (AxioCam HRm; Zeiss) at RT.

Quantification and statistical analysis

Droplets combined from three randomly selected fields (60.99 × 45.69 or 89.53 × 67.08 μm) for each reaction were used for determining droplet size. To examine droplet fusion events, ≥100 fusion events were detected in at least three individual experiments. For FRAP assays, data from three individual droplets or puncta were selected.

Wang et al.
Material properties of TFEB condensates

Journal of Cell Biology 19 of 21
https://doi.org/10.1083/jcb.202112024

Graph plots and P values (*, $P < 0.05$; **, $P < 0.01$; and ***, $P < 0.001$) were generated using GraphPad Prism 5 software. Statistical comparisons were made using the unpaired Student's *t* test. All data are shown as mean ± SEM.

Online supplemental material

Fig. S1 shows that TFEB condensates exhibit unique physical properties. Fig. S2 shows that small molecules alter the material properties of TFEB droplets. Fig. S3 shows that small molecules activate lysosomal function and biogenesis. Fig. S4 shows that small molecules activate lysosomal biogenesis in a TFEB-dependent manner. Fig. S5 shows that Ro-3306 treatment promotes autophagy.

References

Banani, S.F., H.O. Lee, A.A. Hyman, and M.K. Rosen. 2017. Biomolecular condensates: Organizers of cellular biochemistry. *Nat. Rev. Mol. Cell Biol.* 18:285–298. https://doi.org/10.1038/nrm.2017.7

Biswas, B., and D.A. Haydon. 1962. The coalescence of droplets stabilised by viscoelastic adsorbed films. *Kolloid-Z Z Polym, Band*. 185:Heft 1. https://doi.org/10.1007/bf01882345

Boeynaems, S., S. Alberti, N.L. Fawzi, T. Mittag, M. Polymenidou, F. Rousseau, J. Schymkowitz, J. Shorter, B. Wolozin, L. Van den Bosch, et al. 2018. Protein phase separation: A new phase in cell biology. *Trends Cell Biol.* 28:420–435. https://doi.org/10.1016/j.tcb.2018.02.004

Boija, A., I.A. Klein, B.R. Sabari, A. Dall'Agnese, E.L. Coffey, A.V. Zamudio, C.H. Li, K. Shrinivas, J.C. Manteiga, N.M. Hannett, et al. 2018. Transcription factors activate genes through the phase-separation capacity of their activation domains. *Cell*. 175:1842–1855.e16. https://doi.org/10.1016/j.cell.2018.10.042

Brangwynne, C.P., C.R. Eckmann, D.S. Courson, A. Rybarska, C. Hoege, J. Gharakhani, F. Jülicher, and A.A. Hyman. 2009. Germline P granules are liquid droplets that localize by controlled dissolution/condensation. *Science*. 324:1729–1732. https://doi.org/10.1126/science.1172046

Brangwynne, C.P., T.J. Mitchison, and A.A. Hyman. 2011. Active liquid-like behavior of nucleoli determines their size and shape in Xenopus laevis oocytes. *Proc. Natl. Acad. Sci. USA*. 108:4334–4339. https://doi.org/10.1073/pnas.1017150108

Chen, D., Z. Wang, Y. G. Zhao, H. Zheng, H. Zhao, N. Liu, and H. Zhang. 2020. Inositol polyphosphate multikinase inhibits liquid-liquid phase separation of TFEB to negatively regulate autophagy activity. *Dev. Cell*. 55:588–602.e7. https://doi.org/10.1016/j.devcel.2020.10.010

Cho, W.K., J.H. Spille, M. Hecht, C. Lee, C. Li, V. Grube, and I.I. Cisse. 2018. Mediator and RNA polymerase II clusters associate in transcription-dependent condensates. *Science*. 361:412–415. https://doi.org/10.1126/science.aar4199

Chong, S.S., C. Dugast-Darzacq, Z. Liu, P. Dong, G.M. Dailey, C. Cattoglio, A. Heckert, S. Banala, L. Lavis, X. Darzacq et al. 2018. Imaging dynamic and selective low-complexity domain interactions that control gene transcription. *Science*. 361:eaar2555.

Cortes, C.J., H.C. Miranda, H. Frankowski, Y. Batlevi, J.E. Young, A. Le, N. Ivanov, B. L. Sopher, C. Carromeu, A.R. Muotri, et al. 2014. Polyglutamine-expanded androgen receptor interferes with TFEB to elicit autophagy defects in SBMA. *Nat. Neurosci.* 17:1180–1189. https://doi.org/10.1038/nn.3787

Cullup, T., A.L. Kho, C. Dionisi-Vici, B. Brandmeier, F. Smith, Z. Urry, M.A. Simpson, S. Yau, E. Bertini, V. McClelland, et al. 2013. Recessive mutations in EPG5 cause Vici syndrome, a multisystem disorder with defective autophagy. *Nat. Genet.* 45:83–87. https://doi.org/10.1038/ng.2497

Decressac, M., B. Mattsson, P. Weikop, M. Lundblad, J. Jakobsson, and A. Björklund. 2013. TFEB-mediated autophagy rescues midbrain dopamine neurons from α-synuclein toxicity. *Proc. Natl. Acad. Sci. USA*. 110:1817–1826. https://doi.org/10.1073/pnas.1305623110

Drelich, J., C. Fang, and C.L. White. 2002. Measurement of interfacial tension in fluid-fluid systems. *Encycl. Surf. Colloid Sci.* 3152–3166.

Eggers, D.K., W.J. Welch, and W.J. Hansen. 1997. Complexes between nascent polypeptides and their molecular chaperones in the cytosol of mammalian cells. *Mol. Biol. Cell*. 8:1559–1573. https://doi.org/10.1091/mbc.8.8.1559

Elbaum-Garfinkle, S., Y. Kim, K. Szczepaniak, C.C.H. Chen, C.R. Eckmann, S. Myong, and C.P. Brangwynne. 2015. The disordered P granule protein LAF-1 drives phase separation into droplets with tunable viscosity and dynamics. *Proc. Natl. Acad. Sci. USA*. 112:7189–7194. https://doi.org/10.1073/pnas.1504822112

Fang, M.Y., S. Markmiller, A.Q. Vu, A. Javaherian, W.E. Dowdle, P. Jolivet, P.J. Bushway, N.A. Castello, A. Baral, M.Y. Chan, et al. 2019. Small-molecule modulation of TDP-43 recruitment to stress granules prevent persistent TDP-43 accumulation in ALS/FTD. *Neuron*. 103:802–819. https://doi.org/10.1016/j.neuron.2019.05.048

Feric, M., N. Vaidya, T.S. Harmon, D.M. Mitrea, L. Zhu, T.M. Richardson, R.W. Kriwacki, R.V. Pappu, and C.P. Brangwynne. 2016. Coexisting liquid phases underlie nucleolar subcompartments. *Cell*. 165:1686–1697. https://doi.org/10.1016/j.cell.2016.04.047

Forkey, J.N., M.E. Quinlan, and Y.E. Goldman. 2000. Protein structural dynamics by single-molecule fluorescence polarization. *Prog. Biophys. Mol. Biol.* 74:1–35. https://doi.org/10.1016/s0079-6107(00)00015-8

Guo, B., Q. Liang, L. Li, Z. Hu, F. Wu, Y. Zhang, Y. Ma, B. Zhao, A.L. Kovács, Z. Zhang, et al. 2014. O-GlcNAc-modification of SNAP-29 regulates autophagosome maturation. *Nat. Cell Biol.* 16:1215–1226. https://doi.org/10.1038/ncb3066

Henninger, J.E., O. Oksuz, K. Shrinivas, I. Sagi, G. LeRoy, M.M. Zheng, J.O. Andrews, A.V. Zamudio, C. Lazaris, N.M. Hannett, et al. 2021. RNA-mediated feedback control of transcriptional condensates. *Cell*. 184:207–225.e24. https://doi.org/10.1016/j.cell.2020.11.030

Hertz, H. 1881. Über die Berührung fester elastischer Korper. *J. Reine Angew.* 92:156–171.

Hnisz, D., K. Shrinivas, R.A. Young, A.K. Chakraborty, and P.A. Sharp. 2017. A phase separation model for transcriptional control. *Cell*. 169:13–23. https://doi.org/10.1016/j.cell.2017.02.007

Humphries, W.H., and C.K. Payne. 2012. Imaging lysosomal enzyme activity in live cells using self-quenched substrates. *Anal. Biochem.* 424:178–183. https://doi.org/10.1016/j.ab.2012.02.033

Jia, J., A. Claude-Taupin, Y. Gu, S.W. Choi, R. Peters, B. Bissa, M.H. Mudd, L. Allers, S. Pallikkuth, K.A. Lidke, et al. 2020. Galectin-3 coordinates a

cellular system for lysosomal repair and removal. *Dev. Cell.* 52:69–87.e8. https://doi.org/10.1016/j.devcel.2019.10.025

Juan, G., F. Traganos, W.M. James, J.M. Ray, M. Roberge, D.M. Sauve, H. Anderson, and Z. Darzynkiewicz. 1998. Histone H3 phosphorylation and expression of cyclins A and B1 measured in individual cells during their progression through G2 and mitosis. *Cytometry.* 32:71–77. .

Kaganovich, D. 2017. There is an inclusion for that: Material properties of protein granules provide a platform for building diverse cellular functions. *Trends Biochem. Sci.* 42:765–776. https://doi.org/10.1016/j.tibs.2017.08.002

Kimura, S., T. Noda, and T. Yoshimori. 2007. Dissection of the autophagosome maturation process by a novel reporter protein, tandem fluorescenttagged LC3. *Autophagy.* 3:452–460. https://doi.org/10.4161/auto.4451

Kwon, I., M. Kato, S. Xiang, L. Wu, P. Theodoropoulos, H. Mirzaei, T. Han, S. Xie, J.L. Corden, and S.L. McKnight. 2013. Phosphorylation-regulated binding of RNA polymerase II to fibrous polymers of low-complexity domains. *Cell.* 155:1049–1060. https://doi.org/10.1016/j.cell.2013.10.033

Li, Y., M. Xu, X. Ding, C. Yan, Z. Song, L. Chen, X. Huang, X. Wang, Y. Jian, G. Tang, et al. 2016. Protein kinase C controls lysosome biogenesis independently of mTORC1. *Nat. Cell Biol.* 18:1065–1077. https://doi.org/10.1038/ncb3407

Martina, J.A., and R. Puertollano. 2013. Rag GTPases mediate amino acid–dependent recruitment of TFEB and MITF to lysosomes. *J. Cell Biol.* 200:475–491. https://doi.org/10.1083/jcb.201209135

Martina, J.A., and R. Puertollano. 2018. Protein phosphatase 2A stimulates activation of TFEB and TFE3 transcription factors in response to oxidative stress. *J. Biol. Chem.* 293:12525–12534. https://doi.org/10.1074/jbc.RA118.003471

Martini-Stoica, H., Y. Xu, A. Ballabio, and H. Zheng. 2016. The autophagy–lysosomal pathway in neurodegeneration: A TFEB perspective. *Trends Neurosci.* 39:221–234. https://doi.org/10.1016/j.tins.2016.02.002

Medina, D.L., S. Di Paola, I. Peluso, A. Armani, D. De Stefani, R. Venditti, S. Montefusco, A. Scotto-Rosato, C. Prezioso, A. Forrester, et al. 2015. Lysosomal calcium signalling regulates autophagy through calcineurin and TFEB. *Nat. Cell Biol.* 17:288–299. https://doi.org/10.1038/ncb3114

Mizushima, N., T. Yoshimori, and Y. Ohsumi. 2011. The role of Atg proteins in autophagosome formation. *Annu. Rev. Cell Dev. Biol.* 27:107–132. https://doi.org/10.1146/annurev-cellbio-092910-154005

Nakamura, S., S. Shigeyama, S. Minami, T. Shima, S. Akayama, T. Matsuda, A. Esposito, G. Napolitano, A. Kuma, T. Namba-Hamano, et al. 2020. LC3 lipidation is essential for TFEB activation during the lysosomal damage response to kidney injury. *Nat. Cell Biol.* 22:1252–1263. https://doi.org/10.1038/s41556-020-00583-9

Nakatogawa, H. 2020. Mechanisms governing autophagosome biogenesis. *Nat. Rev. Mol. Cell Biol.* 21:439–458.

Noda, N.N., Z. Wang, and H. Zhang. 2020. Liquid–liquid phase separation in autophagy. *J. Cell Biol.* 219:e202004062. https://doi.org/10.1083/jcb.202004062

Nott, T.J., E. Petsalaki, P. Farber, D. Jervis, E. Fussner, A. Plochowietz, T.D. Craggs, D.P. Bazett-Jones, T. Pawson, J.D. Forman-Kay, et al. 2015. Phase transition of a disordered nuage protein generates environmentally responsive membraneless organelles. *Mol. Cell.* 57:936–947. https://doi.org/10.1016/j.molcel.2015.01.013

Odle, R.I., S.A. Walker, D. Oxley, A.M. Kidger, K. Balmanno, R. Gilley, H. Okkenhaug, O. Florey, N.T. Ktistakis, and S.J. Cook. 2020. An mTORC1-to-CDK1 switch maintains autophagy suppression during mitosis. *Mol. Cell.* 77:228–240.e7. https://doi.org/10.1016/j.molcel.2019.10.016

Puertollano, R., S.M. Ferguson, J. Brugarolas, and A. Ballabio. 2018. The complex relationship between TFEB transcription factor phosphorylation and subcellular localization. *EMBO J.* 37:e98804. https://doi.org/10.15252/embj.201798804

Raben, N., and R. Puertollano. 2016. TFEB and TFE3: Linking lysosomes to cellular adaptation to stress. *Annu. Rev. Cell Dev. Biol.* 32:255–278. https://doi.org/10.1146/annurev-cellbio-111315-125407

Rubinsztein, D.C., M. DiFiglia, N. Heintz, R.A. Nixon, Z.H. Qin, B. Ravikumar, L. Stefanis, and A. Tolkovsky. 2005. Autophagy and its possible roles in nervous system diseases, damage and repair. *Autophagy.* 1:11–22. https://doi.org/10.4161/auto.1.1.1513

Sabari, B.R., A. Dall'Agnese, A. Boija, I.A. Klein, E.L. Coffey, K. Shrinivas, B.J. Abraham, N.M. Hannett, A.V. Zamudio, J.C. Manteiga, et al. 2018. Coactivator condensation at super-enhancers links phase separation and gene control. *Science.* 361:eaar3958. https://doi.org/10.1126/science.aar3958

Settembre, C., C. Di Malta, V.A. Polito, M. Garcia Arencibia, F. Vetrini, S. Erdin, S.U. Erdin, T. Huynh, D. Medina, P. Colella, et al. 2011. TFEB links autophagy to lysosomal biogenesis. *Science.* 332:1429–1433. https://doi.org/10.1126/science.1204592

Settembre, C., R. Zoncu, D.L. Medina, F. Vetrini, S. Erdin, S. Erdin, T. Huynh, M. Ferron, G. Karsenty, M.C. Vellard, et al. 2012. A lysosome-to-nucleus signalling mechanism senses and regulates the lysosome via mTOR and TFEB. *EMBO J.* 31:1095–1108. https://doi.org/10.1038/emboj.2012.32

Shen, Y., D. Guan, D. Serien, S. Takeuchi, P. Tong, L. Yobas, and P. Huang. 2017. Mechanical characterization of microengineered epithelial cysts by using atomic force microscopy. *Biophys. J.* 112:398–409. https://doi.org/10.1016/j.bpj.2016.12.026

Shin, Y., and C.P. Brangwynne. 2017. Liquid phase condensation in cell physiology and disease. *Science.* 357:eaaf4382. https://doi.org/10.1126/science.aaf4382

Smith, S.B., Y. Cui, and C. Bustamante. 1996. Overstretching B-DNA: The elastic response of individual double-stranded and single-stranded DNA molecules. *Science.* 271:795–799. https://doi.org/10.1126/science.271.5250.795

Song, J.X., J. Liu, Y. Jiang, Z.Y. Wang, and M. Li. 2021. Transcription factor EB: An emerging drug target for neurodegenerative disorders. *Drug Discov. Today.* 26:164–172. https://doi.org/10.1016/j.drudis.2020.10.013

Sonnichsen, C., and A.P. Alivisatos. 2005. Gold nanorods as novel nonbleaching plasmon-based orientation sensors for polarized single-particle microscopy. *Nano Lett.* 5:301–304. https://doi.org/10.1021/nl048089k

Su, X., J.A. Ditlev, E. Hui, W. Xing, S. Banjade, J. Okrut, D.S. King, J. Taunton, M.K. Rosen, and R.D. Vale. 2016. Phase separation of signaling molecules promotes T cell receptor signal transduction. *Science.* 352:595–599. https://doi.org/10.1126/science.aad9964

Tadros, T.F. 2013. Emulsion Formation and Stability. Wiley-VCH Verlag GmbH & Co. KGaA. 1–75. https://doi.org/10.1002/9783527647941.ch1

Vassilev, L.T., C. Tovar, S. Chen, D. Knezevic, X. Zhao, H. Sun, D.C. Heimbrook, and L. Chen. 2006. Selective small-molecule inhibitor reveals critical mitotic functions of human CDK1. *Proc. Natl. Acad. Sci. USA.* 103:10660–10665. https://doi.org/10.1073/pnas.0600447103

Wang, Z., G. Miao, X. Xue, X. Guo, C. Yuan, Z. Wang, G. Zhang, Y. Chen, D. Feng, J. Hu, and H. Zhang. 2016. The vici syndrome protein EPG5 Is a Rab7 effector that determines the fusion specificity of autophagosomes with late endosomes/lysosomes. *Mol. Cell.* 63:781–795. https://doi.org/10.1016/j.molcel.2016.08.021

Wang, Z., G. Zhang, and H. Zhang. 2019. Protocol for analyzing protein liquid–liquid phase separation. *Biophys. Rep.* 5:1–9. https://doi.org/10.1007/s41048-018-0078-7

Wheeler, R.J., H.O. Lee, I. Poser, A. Pal, T. Doeleman, S. Kishigami, S. Kour, E.N. Anderson, L. Marrone, A. Murthy, et al. 2019. Small molecules for modulating protein driven liquid–liquid phase separation in treating neurodegenerative disease. *bioRxiv.* https://doi.org/10.1101/721001

Xu, D., Y. He, and E.S. Yeung. 2014. Direct observation of the orientation dynamics of single protein-coated nanoparticles at liquid/solid interfaces. *Angew. Chem. Int. Ed. Engl.* 53:6951–6955. https://doi.org/10.1002/ange.201400025

Zhang, G., Z. Wang, Z. Du, and H. Zhang. 2018. mTOR regulates phase separation of PGL granules to modulate their autophagic degradation. *Cell.* 174:1492–1506.e22. https://doi.org/10.1016/j.cell.2018.08.006

Zhang, H., S. Elbaum-Garfinkle, E.M. Langdon, N. Taylor, P. Occhipinti, A.A. Bridges, C.P. Brangwynne, and A.S. Gladfelter. 2015. RNA controls PolyQ protein phase transitions. *Mol. Cell.* 60:220–230. https://doi.org/10.1016/j.molcel.2015.09.017

Zhao, Y.G., P. Codogno, and H. Zhang. 2021. Machinery, regulation and pathophysiological implications of autophagosome maturation. *Nat. Rev. Mol. Cell Biol.* 22:733–750. https://doi.org/10.1038/s41580-021-00392-4

Zhao, Y.G., and H. Zhang. 2018. formation and maturation of autophagosomes in higher eukaryotes: A social network. *Curr. Opin. Cell Biol.* 53:29–36. https://doi.org/10.1016/j.ceb.2018.04.003

Zhao, Y.G., and H. Zhang. 2019. Autophagosome maturation: An epic journey from the ER to lysosomes. *J. Cell Biol.* 218:757–770. https://doi.org/10.1083/jcb.201810099

Zhao, Y.G., and H. Zhang. 2020. Phase separation in membrane biology: The interplay between membrane-bound organelles and membraneless condensates. *Dev. Cell.* 55:30–44. https://doi.org/10.1016/j.devcel.2020.06.033

Zhou, M., W. Li, J. Li, L. Xie, R. Wu, L. Wang, S. Fu, W. Su, J. Hu, J. Wang, and P. Li. 2020. Phase-separated condensate-aided enrichment of biomolecular interactions for high-throughput drug screening in test tubes. *J. Biol. Chem.* 295:11420–11434. https://doi.org/10.1074/jbc.RA120.012981

Zhu, G., J. Xie, W. Kong, J. Xie, Y. Li, L. Du, Q. Zheng, L. Sun, M. Guan, H. Li, et al. 2020. Phase separation of disease-associated SHP2 mutants underlies MAPK hyperactivation. *Cell.* 183:490–502.e18. https://doi.org/10.1016/j.cell.2020.09.002
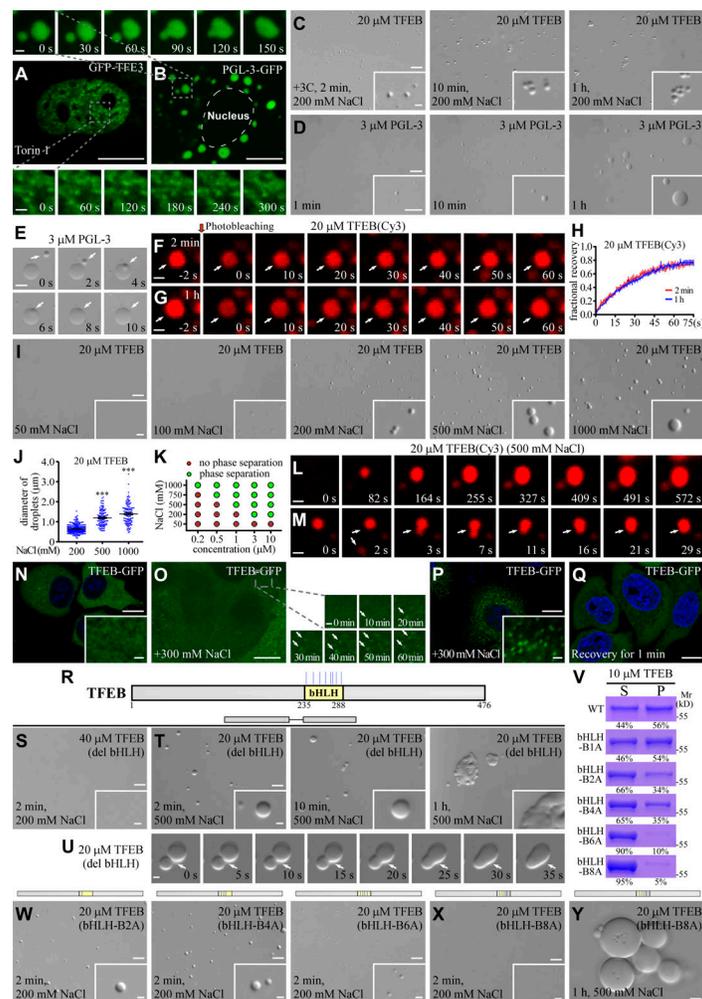
Supplemental material

Figure S1. **TFEB condensates exhibit unique physical properties. (A and B)** Time-lapse experiments show that GFP-TFE3 forms puncta in the nucleus of Torin 1-treated HeLa cells, and these puncta rarely fuse with each other (A). PGL-3-GFP forms large punctate structures that undergo extensive fusion in the cytosol of HeLa cells (B). **(C)** DIC images showing that 20 µM TFEB forms droplets in a 200 mM NaCl buffer 2 min after LLPS induction. The size of TFEB droplets was only slightly increased at 10 min after phase induction, and remains unchanged from 10 min to 1 h. The droplets gradually cluster with time. **(D)** DIC images showing LLPS of PGL-3 in 150 mM NaCl buffer. The PGL-3 droplets fuse with each other upon encounter and their size continues to increase with time. **(E)** Time-lapse images showing fusion of PGL-3 droplets (arrows) in buffer containing 150 mM NaCl. **(F–H)** FRAP analysis of TFEB(Cy3) signal in droplets (arrows) formed in a buffer containing 200 mM NaCl at 2 min (F) and 1 h (G) after LLPS induction. Quantification of the FRAP data is shown as mean ± SEM (n = 3) in H. The fluorescence signals were difficult to bleach, which suggests that molecules are highly dynamic in the droplets. **(I)** DIC images showing that 20 µM TFEB fails to form droplets at 2 min after LLPS induction in buffer containing 50 mM NaCl, but undergoes LLPS in buffer containing higher concentrations of NaCl. The droplet size increases as the NaCl concentration increases from 100 mM to 1,000 mM. **(J)** Column scatter charts show quantification of TFEB droplet size in reactions containing different concentrations of NaCl. Data are shown as mean ± SEM of droplets combined from three fields (60.99 × 45.69 µm) for each reaction (n = 232, 115, and 122 for droplets in 200, 500, and 1,000 mM NaCl buffer, respectively). ***, $P < 0.001$. **(K)** Phase diagram illustrating LLPS of TFEB at various protein and NaCl concentrations. **(L and M)** Cy3-labeled TFEB droplets grow with time in a buffer containing 500 mM NaCl (L). Small droplets (arrows) sometimes undergo fusion upon encounter (M). The fusion events are rare. The time point of the first image is defined as "0 s." **(N)** TFEB-GFP is diffusely localized in the cytoplasm of HeLa cells under normal growth conditions. **(O)** Time-lapse images showing that TFEB-GFP forms punctate structures (arrows) in the cytoplasm in cells after the growth medium is supplemented with 300 mM NaCl. **(P and Q)** TFEB-GFP forms a large number of puncta in the cytoplasm when the growth medium is supplemented with 300 mM NaCl for 30 min (P). The puncta quickly disappear after the high salt medium is replaced with normal medium (Q). **(R)** Schematic illustration of the bHLH domain in TFEB, and the distribution of positively charged residues in the bHLH domain which are mutated in this study. The positively charged residues Arg(R)/Lys(K) are labeled by blue colored vertical lines. **(S)** 40 µM TFEB(del bHLH) fails to undergo LLPS in a buffer containing 200 mM NaCl at 2 min after LLPS induction. **(T and U)** DIC images showing that 20 µM TFEB(del bHLH) forms droplets in 500 mM NaCl buffer from 2 min to 1 h after LLPS induction (T). U shows time-lapse images of two encountering TFEB(del bHLH) droplets (arrows) which undergo partial fusion with time and do not relax into a spherical structure during the time of examination. The time point of the first image is defined as "0 s." **(V)** The percentage of TFEB protein partitioned into pellets in sedimentation assays. Droplets were induced in a buffer containing 200 mM NaCl. S, supernatant; P, pellet. The mutations in TFEB are: K237A for bHLH-B1A, K237A/R247A for bHLH-B2A, K237A/R247A/K256A/K264A for bHLH-B4A, K237A/R247A/K256A/K264A/K274A/R286A for bHLH-B6A and K237A/R247A/K256A/K264A/R271A/K274A/K279A/R286A for bHLH-B8A. **(W and X)** DIC images showing the droplets formed by 20 µM of various mutant TEFB proteins at 2 min after induction in a buffer containing 200 mM NaCl. **(Y)** DIC images showing that large TFEB(bHLH-B8A) droplets are juxtaposed but not fused after LLPS induction for 1 h in a system containing 20 µM protein in 500 mM NaCl buffer. Scale bars: D, 20 µm; A, B, E, N–Q, and insert in D, 10 µm; C, I, S, T, and W–Y, 5 µm; F, G, L, M, and U, 1 µm; inserts in C, I, N, P, S, T, W, and X and enlarged figures in A, B, and O, 1 µm. Source data are available for this figure: SourceDataFS1.
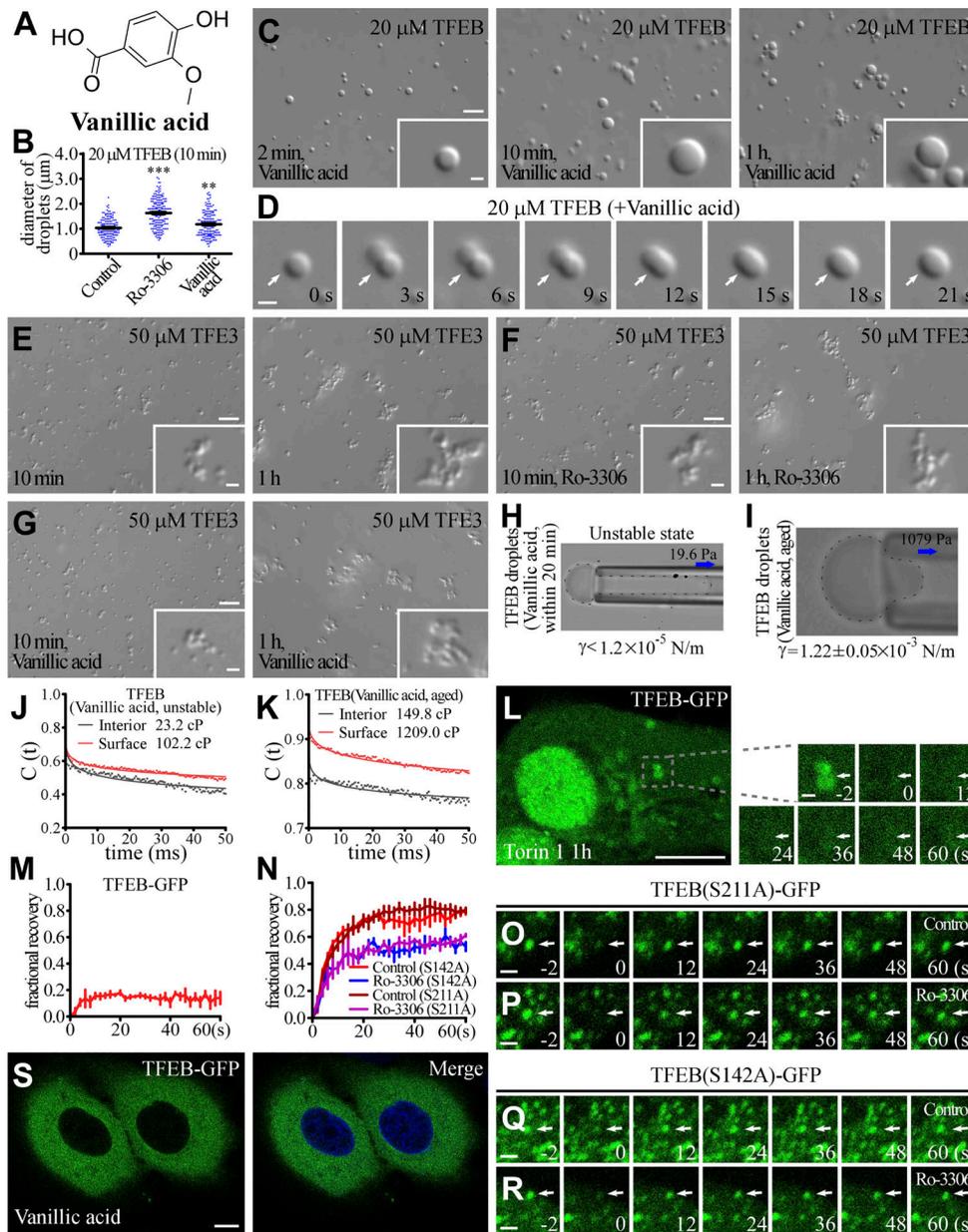
Figure S2. **Small molecules alter the material properties of TFEB droplets. (A)** Two-dimensional structure of Vanillic acid. **(B)** Column scatter charts of the diameters of TFEB droplets formed at 10 min after induction in the absence and presence of 50 μM Ro-3306 or Vanillic acid. Data are shown as mean ± SEM of droplets combined from three fields (89.53 μm × 67.08 μm) for each reaction (n = 150, 184, and 165 for TFEB droplets in the control, Ro-3306 and Vanillic acid systems, respectively). **, $P < 0.01$; ***, $P < 0.001$. **(C and D)** DIC images showing that 20 μM TFEB forms droplets from 2 min to 1 h after LLPS induction in 500 mM NaCl buffer supplemented with 50 μM Vanillic acid (C). D shows time-lapse images of two encountering TFEB droplets undergoing fusion (arrows) with time. The time point of the first image is defined as "0 s." **(E–G)** DIC images showing that 50 μM TFE3 forms droplets from 2 min to 1 h after LLPS induction in 500 mM NaCl buffer in the absence (E) and presence of 100 μM Ro-3306 (F) and Vanillic acid (G). Addition of Ro-3306 and Vanillic acid has no effect on the size and fusion propensity of TFE3 droplets. **(H and I)** Representative pictures of the micropipette experiments for newly formed (H) and aged (I) TFEB droplets in 500 mM NaCl buffer supplemented with 100 μM Vanillic acid. 19.6 and 1,079 Pa of negative pressure was used to draw out the surface of newly formed and aged TFEB droplets, respectively. The interfacial tension for newly formed droplets is estimated and shown underneath, and the calculated interfacial tension for aged droplets is shown underneath as mean ± SEM (n = 6). The droplet shown in H was not still, and kept moving into the micropipette; it was completely drawn into the micropipette within seconds. **(J and K)** Autocorrelation decay curves (solid lines) reflect the rotational behavior of AuNRs in droplets. The calculated apparent viscosity, which is corrected with the viscosity of the solution, is shown at the top. Rotational tracks of the AuNRs in the interior and on the surface were obtained from the same droplets for newly formed (J) and aged (K) TFEB droplets in 500 mM NaCl buffer supplemented with 100 μM Vanillic acid. **(L and M)** FRAP analysis of the TFEB-GFP signal on lysosomes (arrows) in the cytoplasm of Torin 1-treated HeLa cells (L). M shows quantification of the FRAP data for L. Data are shown as mean ± SEM (n = 3) in M. **(N–R)** FRAP analysis of TFEB(S211A)-GFP (O and P) and TFEB(S142A)-GFP (Q and R) signals in the punctate structures (arrows) in the nucleus of control and Ro-3306-treated HeLa cells. N shows quantification of the FRAP data for O–R. Data are shown as mean ± SEM (n = 3) in N. **(S)** Treatment with 10 μM Vanillic acid causes no change in the distribution of TFEB-GFP in HeLa cells stably expressing TFEB-GFP. The nuclei of HeLa cells were stained by DAPI (blue channel). Scale bars: L and S, 10 μm; C and E–G, 5 μm; D, O–R, enlarged figures in L, and inserts in C and E–G, 1 μm.

Wang et al.
Material properties of TFEB condensates

Journal of Cell Biology S3
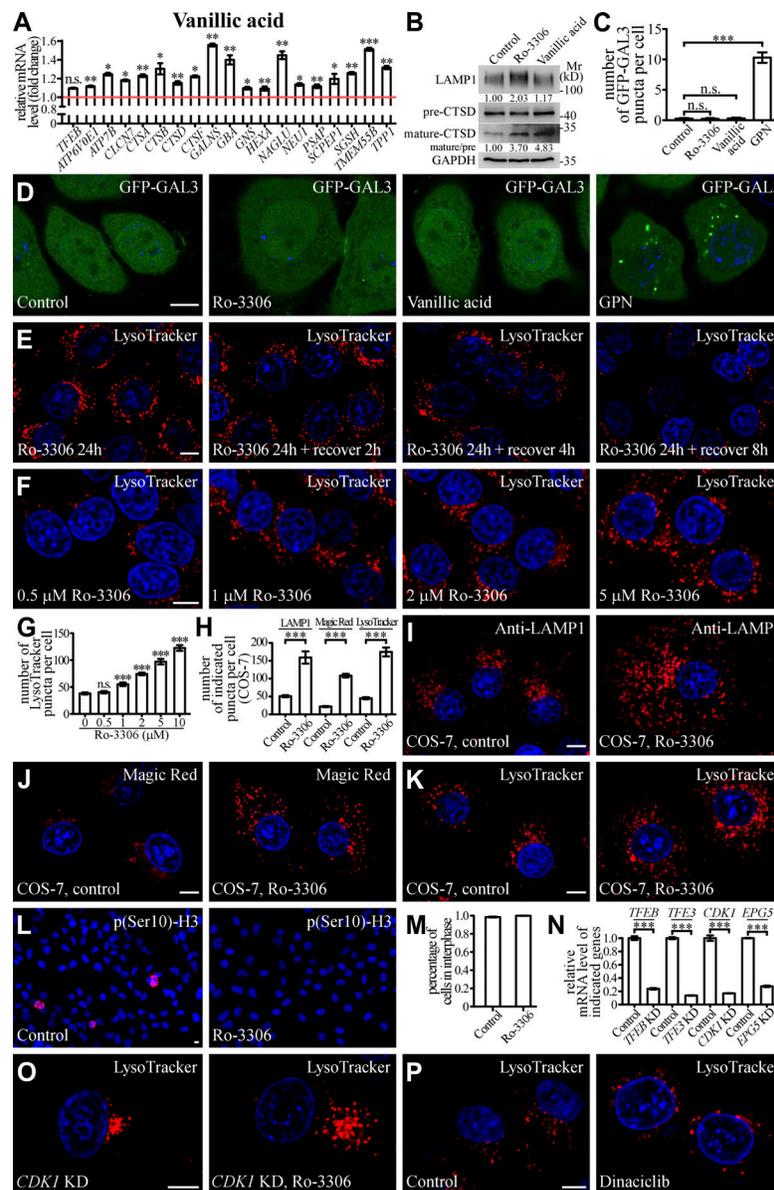https://doi.org/10.1083/jcb.202112024

Figure S3. **Small molecules activate lysosomal function and biogenesis. (A)** qRT-PCR assays showing upregulation of mRNA levels of lysosomal genes in HeLa cells treated with 10 µM Vanillic acid. The genes are *TFEB*, *ATP6V0E1*, *ATP7B*, *CLCN7*, *CTSA*, *CTSB*, *CTSD*, *CTSF*, *GALNS*, *GBA*, *GNS*, *HEXA*, *NAGLU*, *NUE1*, *PSAP*, *SCPEP1*, *SGSH*, *TMEM55B*, and *TPP1*. The level of the corresponding mRNA in control cells is set to 1.0. Data (normalized by *GAPDH* level) are shown as mean ± SEM (*n* = 3 for each bar). *, P < 0.05; **, P < 0.01; *** P < 0.001. **(B)** Immunoblotting assays showing protein levels of LAMP1, and precursor and mature forms of CTSD in control and Ro-3306-treated HeLa cells. Quantifications of LAMP1 level (normalized by GAPDH level) and the ratio of mature CTSD/precursor CTSD are shown underneath. **(C and D)** The number of damaged lysosomes labeled by GFP-GAL3 in control HeLa cells and HeLa cells treated with 10 µM Ro-3306, 10 µM Vanillic acid, or 100 µM GPN (D). GPN treatment results in generation of damaged lysosomes that can be labeled by GFP-GAL3 ([Jia et al., 2020](#)), and was used as a positive control. C shows quantification of the number of GFP-GAL3 puncta per cell. Data are shown as mean ± SEM (*n* = 30 cells for each bar). ***, P < 0.001. **(E)** After Ro-3306 is washed out, the number of LysoTracker-stained lysosomes in 10 µM Ro-3306-treated HeLa cells gradually decreases to basal level within 8 h. **(F and G)** Lysosomal biogenesis shown by LysoTracker staining in HeLa cells treated with Ro-3306 at various concentrations (F). G shows quantification of the number of LysoTracker puncta per cell in control cells and cells treated with various concentrations of Ro-3306. Data are shown as mean ± SEM (*n* = 30 for each bar). ***, P < 0.001. **(H–K)** Compared to control cells, the number of lysosomal structures labeled by anti-LAMP1 antibody (I), Magic Red (J) and LysoTracker (K) is higher in COS-7 cells treated with 10 µM Ro-3306. Lysosomes become more dispersed in Ro-3306 treated cells. H shows quantification of the number of LAMP1, Magic Red and LysoTracker puncta per cell in control and Ro-3306-treated cells. Data are shown as mean ± SEM (*n* = 21, 10, 30, 19, 30, and 26 cells for LAMP1 in control and Ro-3306-treated cells, Magic Red in control and Ro-3306-treated cells and LysoTracker in control and Ro-3306-treated cells, respectively). ***, P < 0.001. **(L and M)** The majority of control and 10 µM Ro-3306-treated HeLa cells are in interphase. Interphase cells are negative for staining with an anti-p(Ser10)-H3 antibody (L). M shows quantification of the percentage of cells in interphase. Data are shown as mean ± SEM (*n* > 500 cells from at least six independent experiments for each bar). **(N)** qRT-PCR assays showing that mRNA levels of *TFEB*, *TFE3*, *CDK1*, and *EPG5* are effectively depleted by the corresponding siRNAs. The level of the corresponding mRNA in control cells is set to 1.0. Data (normalized by *GAPDH* mRNA level) are shown as mean ± SEM (*n* = 3 for each bar). ***, P < 0.001. **(O and P)** In *CDK1* KD HeLa cells, the number of LysoTracker puncta is significantly increased by treatment with 10 µM Ro-3306 (O). Dinaciclib treatment does not change the number of LysoTracker puncta (P). Scale bars: D–F, I–L, O, and P, 10 µm. Source data are available for this figure: SourceDataFS3.
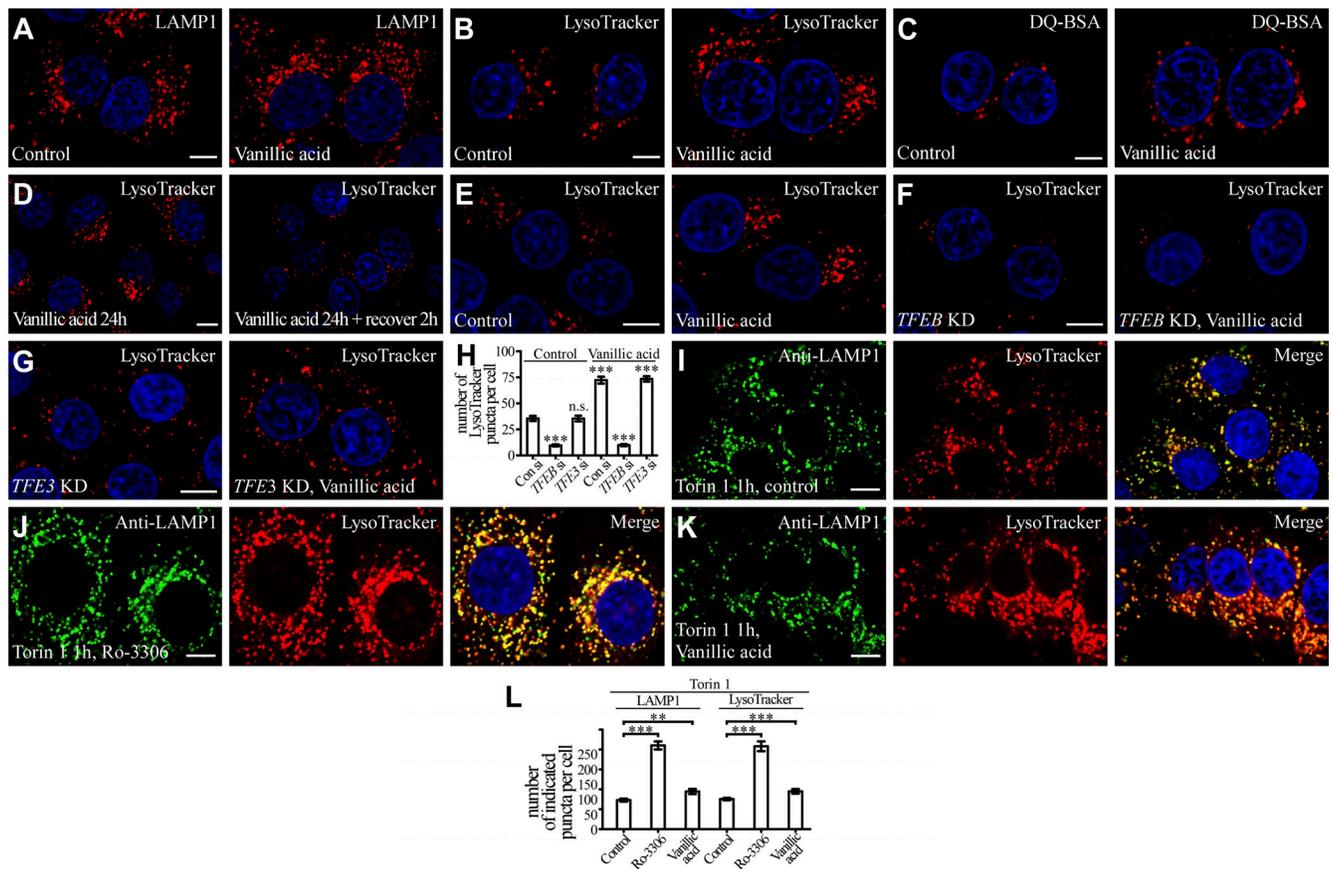
Figure S4. **Small molecules activate lysosomal biogenesis in a TFEB-dependent manner. (A–C)** Compared to control cells, the number of lysosomal structures labeled by anti-LAMP1 antibody (A), LysoTracker (B), and DQ-BSA (C) is higher in HeLa cells treated with 10 µM Vanillic acid. **(D)** The number of LysoTracker-stained lysosomes in 10 µM Vanillic acid-treated HeLa cells gradually decreases to basal level within 2 h. **(E–H)** Compared to control HeLa cells, the number of LysoTracker-stained lysosomal structures is increased by Vanillic acid treatment (E), and this increase is suppressed by simultaneous depletion of TFEB (F). In TFE3 KD HeLa cells, the number of LysoTracker puncta is still significantly increased by 10 µM Vanillic acid treatment (G). H shows quantification of the number of LysoTracker puncta per cell in control and 10 µM Vanillic acid-treated cells with or without TFEB or TFE3 KD. Data are shown as mean ± SEM (n = 20 cells for each bar). ***, P < 0.001. All measured values were statistically compared with the first dataset. **(I–L)** Compared to Torin 1-treated control HeLa cells (I), the number of lysosomal structures labeled by anti-LAMP1 antibody and LysoTracker is further increased by treatment with 10 µM Ro-3306 (J) or Vanillic acid (K). L shows quantification of the number of LAMP1 and LysoTracker puncta per cell in control, Ro-3306- and Vanillic acid–treated cells under Torin1 treatment conditions. Data are shown as mean ± SEM (n = 20 cells for each bar). **, P < 0.01; ***, P < 0.001. Scale bars, A–G and I–K, 10 µm.
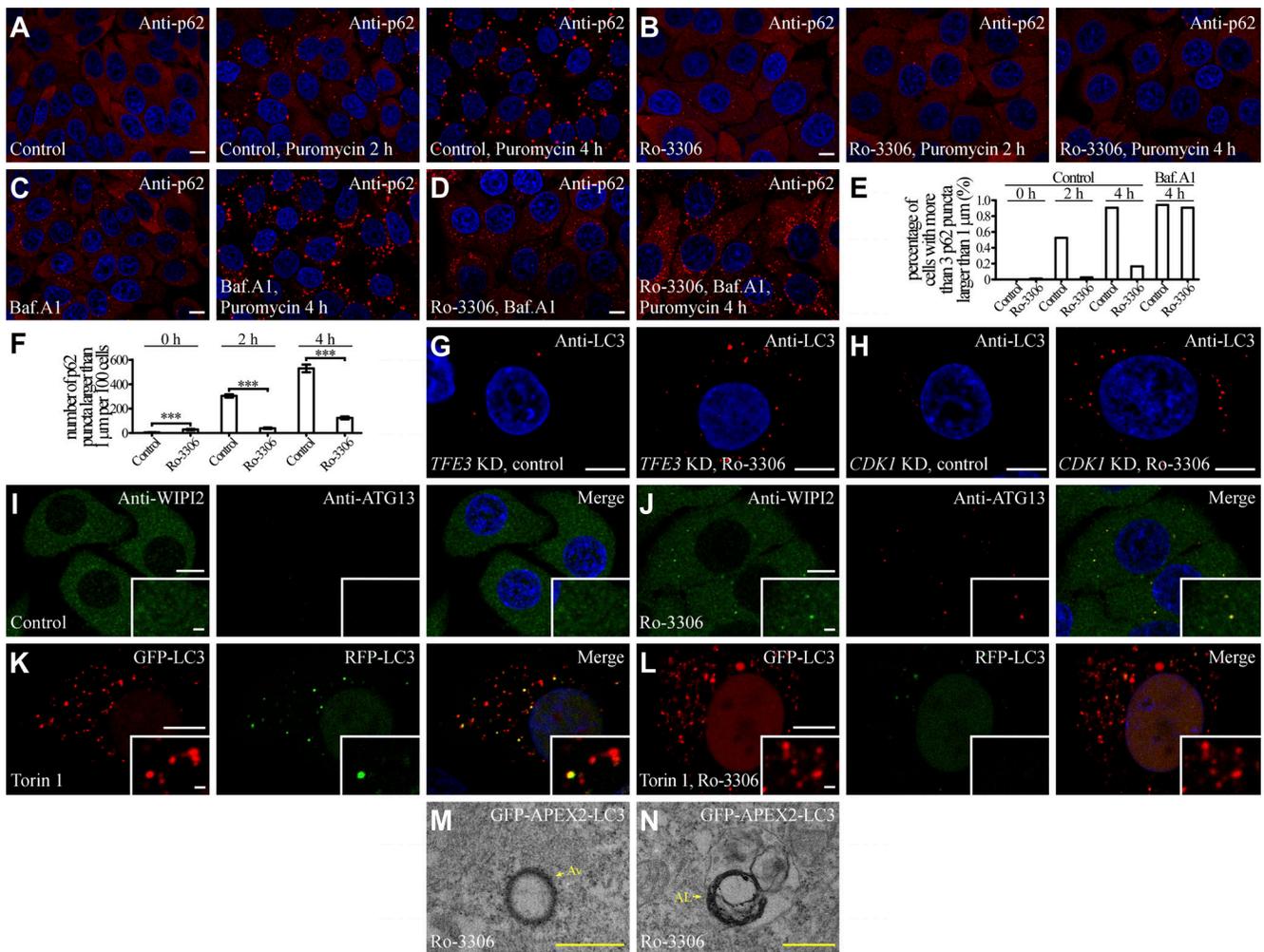
Figure S5. Ro-3306 treatment promotes autophagy. (A–F) In puromycin-treated HeLa cells, p62 (detected by anti-p62 antibody) forms an increasing number of aggregates with time (A). The number of p62 aggregates is dramatically reduced by treatment with 10 µM Ro-3306 (B), and is restored by simultaneous incubation with Baf.A1 (C and D). **(E and F)** Quantification of the percentage of cells with more than three p62 puncta larger than 1 µm (n > 200 cells from at least three independent experiments; E), and the number of p62 puncta larger than 1 µm per 100 cells (F) in control and Ro-3306 treated cells in response to puromycin treatment with the indicated time. Data are shown as mean ± SEM in F (n > 200 cells from at least three independent experiments in F). ***, P < 0.001. **(G and H)** The number of LC3 puncta stained by anti-LC3 is significantly increased by 10 µM Ro-3306 treatment in *TFE3* KD (G) and *CDK1* KD (H) HeLa cells. **(I and J)** Compared to control cells (I), the number of endogenous WIPI2 and ATG13 puncta stained by anti-WIPI2 and anti-ATG13 antibodies is higher in 10 µM Ro-3306-treated HeLa cells (J) under normal conditions. **(K and L)** The RFP-GFP-LC3 assay in control and 10 µM Ro-3306-treated HeLa cells after Torin 1 treatment. Compared to control cells (K), more red-only puncta are formed in Ro-3306-treated cells (L). **(M and N)** TEM images showing that dark APEX2-LC3-derived signals are detected on the membranes of autophagosomes (M) and autolysosomes (N) in 10 µM Ro-3306-treated HeLa cells. AL, autolysosome; Av, autophagosome. Scale bars, A–D and G–L, 10 µm; inserts in I–L, 1 µm; M and N, 500 nm.

Wang et al.
Material properties of TFEB condensates

Journal of Cell Biology   S6
https://doi.org/10.1083/jcb.202112024